ISWFoam: A numerical model for internal solitary wave simulation in continuously stratified fluids

Jingyuan Li[1], Qinghe Zhang[1], Tongqing Chen[1]

[1]State Key Laboratory of Hydraulic Engineering Simulation and Safety, Tianjin University, Tianjin 300072, China

Correspondence to: Qinghe Zhang (qhzhang@tju.edu.cn)

Abstract. A numerical model, ISWFoam, for simulating internal solitary waves (ISWs) in continuously stratified, incompressible, viscous fluids is developed based on a fully three-dimensional (3D) Navier-Stokes equation using the open source code OpenFOAM. This model combines the density transport equation with the Reynolds-averaged Navier-Stokes equation with the Coriolis force, and the model discrete equation adopts the finite volume method. The *k-ω SST* turbulence model has also been modified accordingly to the variable density field. ISWFoam provides two initial wave generation methods to generate an ISW in continuously stratified fluids, including solving the weakly nonlinear models of the extended Korteweg–de Vries (eKdV) equation and the fully nonlinear models of the Dubreil-Jacotin-Long (DJL) equation. Grid independence tests for ISWFoam are performed, considering the accuracy and computing efficiency, the appropriate grid size of the ISW simulation is recommended to be one-one hundred and fiftieth of the characteristic length and one-twenty fifth of the ISW amplitude. Model verifications are conducted through comparisons between the simulated and experimental data for ISW propagation examples over a flat bottom section, including laboratory scale and actual ocean scale, a submerged triangular ridge, a Gaussian ridge and slope. The laboratory test results, including the ISW profile, wave breaking location, ISW arrival time, and the spatial and temporal changes in the mixture region, are well reproduced by ISWFoam. The ISWFoam model with unstructured grids and local mesh refinement can effectively simulate the evolution of ISWs, the ISW breaking phenomenon, waveform inversion of ISWs, and the interaction between ISWs and complex topography.

Key words. OpenFoam, Internal solitary wave tank, Stratified fluid, the DJL equation, Grid independence.

1. Introduction

Internal solitary waves (ISWs) are commonly observed in oceans, particularly on continental shelf

regions, due to strong tidal current flows over large topographic features (Huthnance, 1981), such as in the northern South China Sea (Alford et al., 2010; Alford et al., 2015; Cai et al., 2012). ISWs play an important role in both conveying nutrients from the deep ocean to shallower layers and promoting biological growth (Sandstrom et al., 1984). Additionally, ISWs are a potential threat to the ocean structures of resource exploration, exploitation, and submarine navigation vehicles (Alford et al., 2010; Osborne et al., 1980). A considerable number of studies, which include field measurements, remote sensing, experiments, theoretical analysis and numerical simulations, have been carried out due to the significance of ISWs (Vlasenko et al., 2005; Apel et al., 2006; Alford et al., 2011; Guo et al., 2014).

For numerically simulated ISWs, many models have been adopted, including the Euler equation, the inviscid/viscid incompressible Boussinesq model, the hydrostatic model, the non-hydrostatic model, and the VOF based two-phase flow model. Among these models, the representative hydrostatic models include the Naval Research Laboratory Ocean Nowcast/Forecast System (ONFS) (Ko et al.,2008), the Regional Hallberg Isopycnal Tide Mode (RHIMT) (Hallberg and Rhines, 1996; Hallberg, 1997), and the Ostrovsky-Hunter model. The representative non-hydrostatic models include the Bergen Ocean Model (BOM), the nonhydrostatic Regional Ocean Modeling System model (ROMS), the Stanford Unstructured Nonhydrostatic Terrain-following Adaptive Navier-Stokes Simulator (SUNTANS), and the Massachusetts Institute of Technology general circulation model (MITgcm). For example, Zhang et al (2012) established a variable water depth internal wave numerical model in a continuously stratified fluid system based on the Euler equation. Xu and Stastna (2020) used the viscid incompressible Boussinesq model to study cross-boundary-layer transport (Boegman and Stastna, 2019) by the fissioning process of shoaling ISWs. Lamb (1994) established a non-hydrostatic model, using a second-order projection method developed by Bell and Marcus (1992), which is used for internal wave research including boundary layer instability (Aghsaee et al., 2012), reflection (Lamb, 2009), and the interaction of the tides with the topography (Lamb, 2007; Aghsaee et al., 2010). Diamessis (2005) developed a spectral multidomain penalty method model and correctly reproduced the characteristic vorticity and internal wave structure. Subich et al (2013) developed a spectral collocation method for the solution of the Navier–Stokes equations under the Boussinesq approximation, and simulated the internal wave in continuously stratified fluid. Smedstad et al (2003) employed the ONFS model to establish a global ocean real-time forecasting system with an operational eddy resolution of 1/16°, which effectively tracks ocean

eddies, ocean currents and ocean fronts. Simmons et al (2004) employed the RHIMT model to carry out a global numerical simulation of tidal currents, and analyzed the whole process of the conversion rate of barotropic waves into baroclinic waves. Thiem (2011) used the Bergen Ocean Model to explore the bottom boundary layer flow caused by waves beneath a propagating ISW in a two-fluid system. Li and Farmer (2011) employed the Ostrovsky-Hunter model to study the nonlinear evolution of a monochromatic internal wave. Buijsman et al (2010) employed ROMS model to study the asymmetry in solitons to the east and west of Luzon Strait. Zhang et al (2011) used the nonhydrostatic SUNTANS model (Fringer et al., 2006) to study the dynamics of A wave and B wave formation. Rayson et al (2018) used the modified SUNTANS model to study the internal waves around Scott Reef and provided the generation process of internal lee waves. Vlasenko et al (2010) employed the MITgcm model to investigate the baroclinic tidal energy conversion in the area west of the Luzon Strait.

In summary, for continuously stratified fluids in complex ocean environments, numerical simulation has become a leading method for ISW investigations. However, there are presently few versatile numerical models with share code that can accurately simulate the ISW flow around complex topography and submarine navigation vehicles in continuously stratified fluids. Therefore, the main objective of this paper is to develop a solver, referred to as ISWFoam with a modified k-ω SST model that considers the variable density field, which simulates the ISW in continuous density stratification, incompressible and viscous fluids using the finite volume method with unstructured grids based on a fully three-dimensional (3D) Navier-Stokes equation using the OpenFOAM library.

Notably, the open source field operation and manipulation code OpenFOAM®, as an object-oriented C++ open source library that can be used to build a variety of solvers for computational fluid problems based on the finite volume method, is becoming increasingly popular in the computational fluid research community. At present, the official version of OpenFOAM® does not have a solver or boundary conditions for solving the ISW in continuously stratified fluids. Although some researchers simulate ISWs by modifying the OpenFOAM® code, most of these studies are based on a two-fluid system without considering continuous stratification in density, such as Meng and Zhang (2016) and Li et al (2017). Though recent work by Ding et al (2020) and Li et al (2021) considered continuous stratification in density, their wave generation theories does not consider continuous stratification in density. To extensively use of the numerical model of ISWs as a tool in the future, we will develop ISWFoam to

87 simulate the ISW in continuously stratified, incompressible and viscous fluids based on the OpenFOAM

88 library. The turbulence model will consider the variable density field. In addition, ISWFoam will provide

89 two initial methods to generate an ISW in continuously stratified fluids, including solving the weakly

90 nonlinear models of the extended Korteweg-de Vries (eKdV) equation and the fully nonlinear models of

91 the Dubreil-Jacotin-Long (DJL) equation. This approach renders the numerical model suitable for the

92 simulation of ISW flows in complex geometries and topographies. It is worth noting that ISWFoam does

93 not consider the generation process of ISWs, but focuses on the propagation and evolution of ISWs that

94 have already been generated, and the interaction between ISWs and complex structures and topography

95 on field scales.

96   The outline of the paper is described as follows. First, in Section 2, the governing equations for a

97 continuously stratified fluid are presented, and discrete forms of these equations are derived. Then, grid

98 independence tests of the developed ISWFoam model are described in Section 3. Subsequently, in

99 Section 4, a series of test cases are presented to verify the model. Simulation examples at the field scale

100 in Section 5. Finally, the conclusions are drawn in Section 6.

101 **2. ISWFoam: A three-dimensional numerical solver for ISWs in a continuously stratified fluid**

102 **2.1 Governing equations**

103   We present an ISW numerical model by solving the motion of a three-dimensional, viscous,

104 incompressible fluid with the Boussinesq approximation and rigid lid hypothesis. The governing

105 equations of the model are

106 $$\nabla \cdot \mathbf{U} = 0, \tag{1}$$

107 $$\frac{\partial \mathbf{U}}{\partial t} + (\mathbf{U} \cdot \nabla)\mathbf{U} - \nabla \cdot (\nu_{Eff}\nabla\mathbf{U}) = \mathbf{Q} \quad \mathbf{Q} = \frac{1}{\rho_0}\left(-\nabla p_{\_rgh} - \mathbf{g}\cdot\mathbf{X}\nabla\rho - \Omega e_3\right), \tag{2}$$

108 $$\frac{\partial \rho}{\partial t} + (\mathbf{U}\cdot\nabla)\rho = \nabla\cdot(k\nabla\rho), \tag{3}$$

109 where $\mathbf{U} = (u_i, u_j, u_k)$ is the velocity vector, t is time, ∇ is the gradient operator, $\mathbf{Q}$ is the source term, ρ_0

110 is the reference density, ρ is the density field, $p_{\_rgh}$ is a modified pressure field, $\mathbf{g}$ is the gravitational

111 acceleration vector, and $\mathbf{X}$ is the position vector. ν_{Eff} is the effective kinematic viscosity defined as $\nu_{Eff} =$

112 μ_{Eff}/ρ_0, where μ_{Eff} is the effective dynamic viscosity including the molecular viscosity (μ_l) and turbulent

113 viscosity(μ_t). k is the diffusion coefficient, and its value is the same as the effective dynamic

114 viscosity(μ_{Eff}). Ω is the Coriolis parameter, which is the twice the speed of rotation around the vertical

115 unit vector $e_3 = (0,0,1)$. ISWFoam uses a modified pressure p_rgh instead of a total pressure p, and their

116 relationship is given by

117
$$p_{\_rgh} = p - \rho \mathbf{g} \cdot \mathbf{X}, \ \nabla p_{\_rgh} = \nabla p - \rho \mathbf{g} - \mathbf{g} \cdot \mathbf{X} \nabla \rho, \tag{4}$$

118 To close the above equations, the turbulence model needs to be employed. The two-equation k-ε

119 model is widely used as an effective turbulence model, but it cannot capture the proper behaviour of

120 turbulent boundary layers up to separation due to adverse pressure gradients (Wilcox, 1993). For the

121 above boundary layers separation problem, Bardina et al. (1997) and Menter et al. (2003) suggested the

122 use of the k-ω SST model to obtain substantially more accurate results. Therefore, the turbulence model

123 used in this paper is the k-ω SST model. Notably that in OpenFOAM, the incompressible version for

124 turbulence models does not consider the variable density field, and instead, it treats the density as a

125 constant, such as the k-ω SST model

126
$$\frac{\partial k}{\partial t} + \nabla \cdot (\mathbf{U}k) = \nabla \cdot \left[\left(\nu_{Eff} + \sigma_k \nu_t \right) \nabla k \right] + P_k^* - \beta^* \omega k \tag{5}$$

127
$$\frac{\partial \omega}{\partial t} + \nabla \cdot (\mathbf{U}\omega) = \nabla \cdot \left[\left(\nu_{Eff} + \sigma_\omega \nu_t \right) \nabla \omega \right] + C_\gamma \frac{\omega}{k} P_k - C_\beta \omega^2 + 2(1 - F_1) \frac{\sigma_{\omega2}}{\omega} \nabla k \cdot \nabla \omega \tag{6}$$

128
$$P_k^* = \min(P_k, c_1 C_\mu k \omega) \tag{7}$$

129
$$\nu_t = \frac{a_1 k}{\max \left(a_1 \omega, \sqrt{2} S_t F_2 \right)} \tag{8}$$

130 where k is the turbulent kinetic energy, ω is the specific dissipation rate, P_k is the production term of k,

131 $P_k = \tau^R : \nabla \mathbf{U}$, P_k^* is related to the production term of turbulence kinetic energy P_k in the k equation, ν_t

132 is the turbulent kinematic viscosity, S_t is the mean rate of the flow strain, $S_t = 0.5(\nabla \mathbf{U} + \nabla \mathbf{U}^T)$, the model

133 constants are assigned the values $\beta^* = 0.09$, $a_1 = 0.31$, $c_1 = 10$ and $C_\mu = 0.09$, F_1 and F_2 are blending

134 functions, the value of σ_k, σ_ω, C_γ and C_β are blended using the equation $\Phi = F_1 \Phi_1 + (1 - F_1) \Phi_2$ in which

135 Φ_1 and Φ_2 are given in Table 1.

136
Table 1 Default values for Φ_1 and Φ_2

Φ	σ_k	σ_ω	C_β	C_γ
Φ_1	0.85	0.5	0.075	5/9
Φ_2	1.0	0.856	0.0828	0.44

137

138 Considering the variable density field during the solution process, it is necessary to consider the

139 change in the density field in the turbulence model. Therefore, we modify the turbulence model to

140 consider the change in density, and finally a modified k-ω SST model that considers the change in density

141 is used to close the equation

$$\frac{\partial \rho k}{\partial t} + \nabla \cdot (\rho \mathbf{U} k) = \nabla \cdot \left[\rho \left(\nu_{Eff} + \sigma_k \nu_t \right) \nabla k \right] + \rho P_k^* - \rho \beta^* \omega k \tag{9}$$

$$\frac{\partial \rho \omega}{\partial t} + \nabla \cdot (\rho \mathbf{U} \omega) = \nabla \cdot \left[\rho \left(\nu_{Eff} + \sigma_\omega \nu_t \right) \nabla \omega \right] + C_\gamma \frac{\omega}{k} P_k - C_\beta \rho \omega^2 + 2(1 - F_1) \rho \frac{\sigma_{\omega 2}}{\omega} \nabla k \cdot \nabla \omega \tag{10}$$

2.2 Numerical discretization

146 The governing equations are numerically discretized using the finite volume method based on the

147 C++ open source library of OpenFOAM. The finite volume method requires that Eqs. (2) and (3) are

148 satisfied over the control volume V_P around point P in integral form:

$$\int_{V_P} \int_{\Delta t} \left[\frac{\partial \mathbf{U}}{\partial t} + (\mathbf{U} \cdot \nabla) \mathbf{U} - \nabla \cdot (\nu_{Eff} \nabla \mathbf{U}) \right] dV dt = \int_{V_P} \int_{\Delta t} \mathbf{Q} \, dV dt, \tag{11}$$

$$\int_{V_P} \int_{\Delta t} \left[\frac{\partial \rho}{\partial t} + (\mathbf{U} \cdot \nabla) \rho - \nabla \cdot (k \nabla \rho) \right] dV dt = 0, \tag{12}$$

151 The momentum equation in ISWFoam is solved by constructing a predicted velocity field and then

152 using the Pressure Implicit with Splitting of Operators (PISO) algorithm (Issa, 1986) to modify it. n is

153 defined to represent the current moment. The PISO iteration process is marked as m; when m is equal to

154 zero, it represents the initial moment (t^n).

155 First, only the temporal, convection and diffusion terms appear in the discrete version of the

156 equation momentum, and the other terms are ignored. After this operation, we obtain an explicit

157 expression for the predicted velocity field $\mathbf{U}_P^r$, namely,

$$\frac{\mathbf{U}_P^r - \mathbf{U}_P^n}{\Delta t} V_P + \sum_{f \in \partial V_P} \left(\phi_f^n \mathbf{U}_f^r \right) - \sum_{f \in \partial V_P} \nu_{Eff} \nabla \mathbf{U}_f^r \cdot \mathbf{S}_f = 0, \tag{13}$$

159 where P represents the centre of the grid cell, $\phi_f^n = \mathbf{U}_f^n \cdot \mathbf{S}_f$ is the volume flux at the initial time n and

160 $\mathbf{S}_f$ is the face vector.

161 The solution process requires the velocity on the surface f. Assuming the variation in $\mathbf{U}_f^r$ between

162 the centre P of the grid and the centre N of the adjacent grid, the face values are calculated using a mixture

163 method (blended differencing) of the central scheme (central differencing) and the upwind scheme

164 (upwind differencing) as follows (Jasak, 1996):

165 $$\mathbf{U}_f = (1-\lambda_U)(\mathbf{U}_f)_{UD} + \lambda_U (\mathbf{U}_f)_{CD} \tag{14}$$

166 where

167 $$(\mathbf{U}_f)_{UD} = \begin{cases} \mathbf{U}_P \text{ for } \phi_f \geq 0, \\ \mathbf{U}_N \text{ for } \phi_f < 0, \end{cases} \text{ and } (\mathbf{U}_f)_{CD} = \frac{\mathbf{U}_P + \mathbf{U}_N}{2} \tag{15}$$

168 where N represents the centre of the adjacent grid cells, $\phi_f = \mathbf{U}_f \cdot \mathbf{S}_f$ is volume flux. The limiter λ_U

169 can be selected from several alternatives (OpenFOAM, 2019), including linear, QUICK, vanLeer, etc. In

170 the following derivation process, the vanLeer scheme was used to calculate the velocity of the face centre

171 $$\mathbf{U}_f = \frac{1}{2}(\mathbf{U}_P + \mathbf{U}_N) + \frac{1}{2}\left[\psi(\phi_f)(1-\lambda_U)\right](\mathbf{U}_P - \mathbf{U}_N), \tag{16}$$

172 where $\psi(\phi_f)$ is a step function defined by

173 $$\psi(\phi_f) = \begin{cases} 1 \text{ for } \phi_f \geq 0, \\ -1 \text{ for } \phi_f < 0, \end{cases} \tag{17}$$

174 Inserting Eq. (16) into Eq. (13) yields

175 $$A_P \mathbf{U}_P^r = \sum_{f \in \partial V_P} A_N \mathbf{U}_P^m + \frac{\mathbf{U}_P^n}{\Delta t} = H(\mathbf{U}^m) \tag{18}$$

176 After some manipulation, the quantities A_P and A_N are given as

177 $$A_P = \left\{ \frac{V_P}{\Delta t} + \sum_{f \in \partial V_P} \frac{\phi_f^n}{2}\left[1 + \psi(\phi_f)(1-\lambda_U)\right] + \sum_{f \in \partial V_P} v_{Eff,f} \frac{|\mathbf{S}_f|}{|d|} \right\} \frac{1}{V_P} \tag{19}$$

178 $$A_N = \left\{ -\frac{\phi_f^n}{2}\left[1 - \psi(\phi_f)(1-\lambda_U)\right] + v_{Eff,f} \frac{|\mathbf{S}_f|}{|d|} \right\} \frac{1}{V_P} \tag{20}$$

179 Including the effect of gravity and the Coriolis force in Eq. (18)

180 $$\mathbf{U}_P^r = \frac{H(\mathbf{U}^m)}{A_P} - \frac{(\mathbf{g} \cdot \mathbf{X} \nabla \rho / \rho_0)^n}{A_P} - \frac{(\Omega e_3)^n}{A_P}, \tag{21}$$

181 Notably, that when m is equal to zero, it represents the initial moment n, and the value of the initial

182 moment is known. Therefore, we obtain the predicted velocity field $\mathbf{U}_P^r$ in the first iteration. We define

183 the surface gradient operator ($\nabla \frac{1}{f}$), and the type of gradient operator acting on $\mathbf{U}$ is

184 $\nabla \frac{1}{f}\mathbf{U} = (\mathbf{U}_N^m - \mathbf{U}_P^m)/|d|$, which represents the distance from the centre of the grid N to P. Similarly,

185 the surface gradient operator ($\nabla \frac{1}{f}$) acting on scalar γ is $\nabla \frac{1}{f}\lambda = (\lambda_N^m - \lambda_P^m)/|d|$. The associated flux

186   ($\phi_f = \mathbf{U}_f \cdot \mathbf{S}_f$) is achieved by executing an inner product with a surface vector ($\mathbf{S}_f$) on the left and right

187   parts of Eq. (21), giving

188      $$\phi_f^r = \left(\frac{H(\mathbf{U}^m)}{A_P}\right)_f \cdot \mathbf{S}_f - \left(\left(\frac{1}{A_P}\right)_f (\mathbf{g}\cdot\mathbf{X})_f^n \left(\frac{1}{\rho_0}\nabla_{\frac{1}{f}}\rho\right)^n |\mathbf{S}_f|\right) - \left(\frac{(\Omega e_3)^n}{A_P}\right)_f \cdot \mathbf{S}_f , \qquad (22)$$

189   Eq. (22) completed the flux calculation without considering the influence of the pressure term. The

190   pressure contribution in terms of a flux can be expressed as

191      $$\left(\frac{-\nabla p_{\_rgh}}{\rho_0 A_P}\right)_f \cdot \mathbf{S}_f = \left(\frac{-1}{A_P}\right)_f \left(\frac{1}{\rho_0}\nabla_{\frac{1}{f}}p_{\_rgh}^{m+1}\right)|\mathbf{S}_f| , \qquad (23)$$

192   Then, Eq. (23) is now added to Eq. (22) to yield

193      $$\phi_f^{m+1} = \left(\frac{H(\mathbf{U}^m)}{A_P}\right)_f \cdot \mathbf{S}_f - \left(\left(\frac{1}{A_P}\right)_f (\mathbf{g}\cdot\mathbf{X})_f^n \left(\frac{1}{\rho_0}\nabla_{\frac{1}{f}}\rho\right)^n |\mathbf{S}_f|\right) - \left(\frac{(\Omega e_3)^n}{A_P}\right)_f \cdot \mathbf{S}_f - \left(\frac{1}{A_P}\right)_f \left(\frac{1}{\rho_0}\nabla_{\frac{1}{f}}p_{\_rgh}^{m+1}\right)|\mathbf{S}_f| \qquad (24)$$

194   Combined with Eq. (22), Eq. (24) is simplified and rewritten as

195      $$\phi_f^{m+1} = \phi_f^r - \left(\frac{1}{A_P}\right)_f \left(\frac{1}{\rho_0}\nabla_{\frac{1}{f}}p_{\_rgh}^{m+1}\right)|\mathbf{S}_f| \qquad (25)$$

196   Using conservation of mass, we solve the pressure field $p_{\_rgh}^{m+1}$, which results in

197      $$\sum_{f\in\partial V_P}\left(\frac{1}{A_P}\right)_f \left(\frac{1}{\rho_0}\nabla_{\frac{1}{f}}p_{\_rgh}^{m+1}\right)|\mathbf{S}_f| = \sum_{f\in\partial V_P}\phi_f^r \qquad (26)$$

198   The preconditioned conjugate gradient method is used to solve the linear system constructed by Eq.

199   (26) (OpenFOAM, 2019). After $p_{\_rgh}^{m+1}$ is obtained using Eq. (26), we calculate the volume flux using

200   Eq. (25) for each face. The cell centred velocity fields $\mathbf{U}_P^{m+1}$ are calculated by reconstructing the face

201   velocity flux using the following expression (Deshpande, 2012)

202      $$\mathbf{U}_P^{m+1} = \mathbf{U}_P^r + \left(\frac{1}{A_P}\right)\left(\sum_{f\in\partial V_P}\frac{\mathbf{S}_f\mathbf{S}_f}{|\mathbf{S}_f|}\right)^{-1} \cdot \left(\sum_{f\in\partial V_P}\left(\frac{\phi_f^{m+1} - (\mathbf{U}_P^r)_f \cdot \mathbf{S}_f}{(1/A_P)_f}\right)\frac{\mathbf{S}_f}{|\mathbf{S}_f|}\right) \qquad (27)$$

203   Eq. (27) completes the velocity field calculation of the first iteration step in the PISO algorithm. By

204   converting the identifier *m* to *m*+1, the next PISO iteration is completed and updating the velocity in Eq.

205   (18) with the velocity $\mathbf{U}_P^{m+1}$ calculated from Eq. (27), thereby updating $p_{\_rgh}$, ϕ_f and $\mathbf{U}$. This procedure

206   is performed *M* times to guarantee that the results of the velocity and pressure together conform to the

207   continuity and momentum equations. Considering that PISO iteration levels require more than 1, but

208 typically not more than 4 (OpenFOAM, 2019), we specify that the number of PISO iteration levels is 3

209 in the computations presented in this paper. After completing the three iterations, the converged values

210 are considered the result of the next time step ($n + 1$), namely,

211
$$\phi_f^{n+1} = \phi_f^M, \quad \mathbf{U}_P^{n+1} = \mathbf{U}_P^M, \quad p_{\_rgh}^{n+1} = p_{\_rgh}^M, \tag{28}$$

212 We discretize the convection-diffusion equation of density (12) to obtain

213
$$\frac{V_P}{\Delta t}(\rho_P^{n+1} - \rho_P^n) + \sum(\phi_f^{n+1}\rho_f^{n+1}) = \sum k\left[|\mathbf{S}_f|\frac{\rho_N^{n+1} - \rho_P^{n+1}}{|d|}\right], \tag{29}$$

214 At the end of the iteration procedure, we bring the results of the volume flux into Eq. (29) to

215 calculate the density field at the next time (ρ_P^{n+1}), thereby updating the density field for the next step

216 calculation ($\Delta t = t^{n+2} - t^{n+1}$).

217 **2.3 Initialized field of ISW generation**

218 ISW generation methods mainly include the gravity collapse mechanism, double push-pedals

219 method (Fu et al., 2008), velocity-inlet method (Gao et al., 2012), mass source method (Wang et al.,

220 2018), initialization method, and methods addressing the interaction between tidal current and

221 topography. For example, Hsieh et al (2014) investigated the flow evolution of a depression ISW

222 generated by the gravity collapse mechanism. Cheng et al (2020) studied the interaction between ISWs

223 and a cylinder using the gravity collapse mechanism. The initialization method involves solving the

224 internal solitary wave theory at the initial moment, such as the Korteweg-de Vries (KdV) equation

225 (Grimshaw et al., 2010), the modified KdV (mKdV) equation, the extended KdV (eKdV) equation, the

226 forced KdV equation, the Ostrovsky equation (Li and Farmer, 2011), the Miyata-Choi-Camassa (MCC)

227 model (Miyata 1985 and 1988; Choi and Camassa, 1999), and the Dubreil-Jacotin-Long (DJL) equation

228 (Long, 1953; Turkington, 1991; Brown and Christie, 1997; Dunphy et al., 2011), to obtain the wave

229 surface, velocity field. The method of an interacting between tidal current and terrain that stimulates

230 ISWs is adopted by many scholars, such as Farmer and Smith (1980), Lamb et al (1994), and Shaw et al

231 (2009).

232 In this paper, the method of initializing the field is selected to generate the ISWs. To increase the

233 application range of the ISWFoam model, two initialization methods are provided, including solving the

234 weakly nonlinear models of the eKdV equation (Helfrich and Melville, 2006) and the fully nonlinear

235   models of the DJL equation for continuously stratified fluids (Turkington, 1991; Dunphy et al, 2011).

236   The Dubreil-Jacotin-Long (DJL) equation is expressed as

237
$$\nabla^2 \eta + \frac{N^2(z-\eta)}{c^2}\eta = 0, \quad \eta = 0 \quad \text{at} \quad z = 0, -H$$
$$\eta = 0 \quad \text{at} \quad |x| \to \infty$$
(30)

238   where η is the isopycnal displacement, H is the water depth, c is the propagation speed, N is the definition

239   of the buoyancy frequency, and z is vertical position.

240
$$N^2(z) = -g\frac{d\rho_0(z)}{dz},$$
(31)

241   where $\rho_0(z)$ is the reference density, and g is the gravitational acceleration.

242   By solving the above DJL equation we can obtain η and c, and then through the relationship $\psi = \eta c$,

243   where ψ is the stream function, we can obtain the wave-induced velocity field. We use the DJLES open

244   source package provided by Dunphy et al (2011) to solve the DJL equations. Then we input the initial

245   field calculated by DJLES into OpenFOAM to obtain the initial field required for OpenFOAM numerical

246   simulation.

247   Another theory of ISWFoam model wave generation involves the weakly nonlinear models of the

248   eKdV equation. Using the first order stream function for the DJL equation, we can obtain the well-known

249   KdV equation and further obtain the eKdV equation. For the specific derivation, please refer to the paper

250   by Lamb and Yan (1996). The eKdV equation (Helfrich and Melville, 2006) is

251
$$\frac{\partial \zeta}{\partial t} + (c_0 + c_1\zeta + c_3\zeta^2)\frac{\partial \zeta}{\partial x} + c_2\frac{\partial^3 \zeta}{\partial x^3} = 0,$$
(32)

252
$$c_0^2 = \frac{gh_1h_2(\rho_2 - \rho_1)}{\rho_1h_2 + \rho_2h_1},$$
(33)

253
$$c_1 = -\frac{3c_0}{2}\frac{\rho_1h_2^2 - \rho_2h_1^2}{\rho_1h_1h_2^2 + \rho_2h_1^2h_2},$$
(34)

254
$$c_2 = \frac{c_0}{6}\frac{\rho_1h_1^2h_2 + \rho_2h_1h_2^2}{\rho_1h_2 + \rho_2h_1},$$
(35)

255
$$c_3 = \frac{3c_0}{h_1^2h_2^2}\left[\frac{7}{8}\left(\frac{\rho_1h_2^2 - \rho_2h_1^2}{\rho_1h_2 + \rho_2h_1}\right)^2 - \frac{\rho_1h_2^3 + \rho_2h_1^3}{\rho_1h_2 + \rho_2h_1}\right],$$
(36)

256   where ζ is the isopycnal vertical displacement; h_1 and h_2 are the mean upper and lower layer depths,

257 respectively; ρ_1 and ρ_1 are the fluid densities of the upper and lower layers, respectively. The theoretical

258 solution of Eq. (32) above is

$$\zeta = \frac{a}{B + (1 - B)\cosh^2\left[\lambda_{\text{eKdV}}\left(x - c_{\text{eKdV}}t\right)\right]}, \quad (37)$$

$$\lambda_{\text{eKdV}}^2 = \frac{a}{12c_2}\left(c_1 + \frac{1}{2}c_3a\right), \quad (38)$$

$$c_{\text{eKdV}} = c_0 + \frac{a}{3}\left(c_1 + \frac{1}{2}c_3a\right), \quad (39)$$

$$B = \frac{-ac_3}{2c_1 + ac_3}, \quad (40)$$

$$u_1 = -c_{\text{eKdV}}\frac{\zeta}{h_1 - \zeta}, \quad u_2 = c_{\text{eKdV}}\frac{\zeta}{h_2 + \zeta}, \quad (41)$$

264 where a is the ISW amplitude, λ_{eKdV} is the wavelength, c_{eKdV} is the wave speed, B is an auxiliary parameter,

265 and u_1 and u_2 are the speeds of the upper and lower layers of the fluid, respectively. The waveform and

266 velocity field of the ISWs are solved at the initial moment by the developed function and then assigned

267 to the calculation domain.

268 The vertical profile of the initial density is given by a hyperbolic tangent function profile (Aghsaee

269 et al., 2010)

$$\overline{\rho}(z) = \frac{\rho_1 + \rho_2}{2} - \frac{\rho_2 - \rho_1}{2}\tanh\left(\frac{z - z_{pyc}}{d_{pyc}}\right) \quad (42)$$

271 where z is the vertical position; ρ_1 and ρ_2 are the fluid densities of the upper and lower layers, respectively;

272 z_{pyc} is the location of the centre of the pycnocline; and d_{pyc} is the thickness of the pycnocline. In this paper,

273 unless otherwise specified, the form of the density profile adopts Eq. (42). The internal solitary wave

274 surface is obtained by calculating the gradient of the density field, and the absolute value of the maximum

275 value of the gradient represents the vertical position of the wave surface. Notably, the density profile of

276 the actual ocean is not always hyperbolic, so our model provides a function for users to modify the

277 density profile according to the actual situation.

278 **2.3.1 Comparison between the DJL equation and the eKdV equation**

279 To compare the DJL equation and the eKdV equation, we set up a numerical simulation, which

280 includes a tank that is 15 m long, 1 m wide and has a water depth of 0.5 m. The depths of the upper (h_1)

281 and lower (h_2) layers are 0.1 m and 0.4 m, respectively, the densities of the upper and lower layers are

282   1022 kg/m^3 and 1028 kg/m^3, respectively, the location of the centre of the pycnocline (z_{pyc}) is 0.4 m, the

283   pycnocline thickness (d_{pyc}) is 0.04 m vertically, the initial ISW amplitude (a) is 0.065 m and the location

284   of the centre of ISW is 12.5m. The ISWs propagate from right to left. The measuring point P is set at a

285   position 10m away from the initial ISW. The grid is uniform in the x-direction, y-direction and z-direction,

286   and the sizes are $\Delta x = 1\times10^{-2}$ m, $\Delta y = 1\times10^{-2}$ m and $\Delta z = 1\times10^{-3}$ m, respectively. Slip boundary conditions

287   are applied to the bottom and both sides, while cyclic boundary conditions are assigned to the inlet and

288   outlet boundaries. The top boundary is a rigid lid. The boundary conditions related to the density field

289   are no-flux boundary conditions.

290   Fig. 1 shows the comparison of the horizontal velocity component field when the DJL equation and

291   the eKdV equation are used to generate ISWs. At the initial moment, the ISW generated by the eKdV

292   equation is not as smooth as the ISW generated by the DJL equation, and the horizontal velocity at the

293   interface area is discontinuous as shown in Fig. 1(a) and (b). With the propagation of ISWs, the ISWs

294   generated by the DJL equation are always smooth at the interface area, and the velocity field is always

295   continuous as shown in Fig. 1(a), (c), (e) and (g). Correspondingly, the ISW generated by the eKdV

296   equation gradually produces a gradient in the vertical direction of the horizontal velocity in the interface

297   area, thus, the interface area becomes smooth, and the velocity becomes continuous. Fig. 1(d) shows this

298   evolution process, which is basically completed in 5s as shown in Fig. 1(f). At 50s, the difference between

299   the horizontal velocity fields of the two equations is very small as shown in Fig. 1(g) and (h).
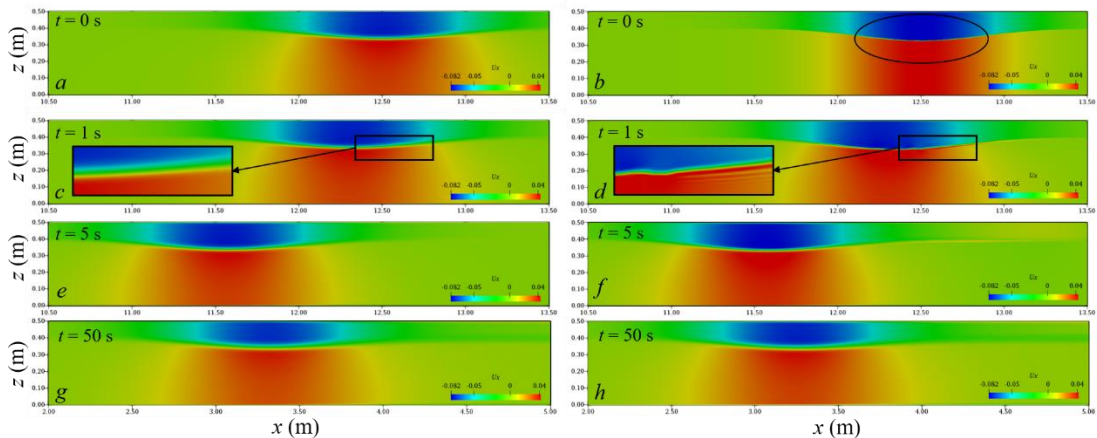
300
301   Figure 1: Comparison chart of the horizontal velocity component field: DJL equation (left) and eKdV equation
302   (right).

303   Fig. 2 shows the comparison of the vertical velocity component field when the DJL equation and

304   the eKdV equation are used to generate ISWs. Since the theoretical solution of the eKdV equation only

305   obtain the average horizontal velocity of the upper and lower layers of the fluid, there is no vertical

306 velocity at the initial moment, as shown in Fig. 2(*b*). With the propagation of ISWs, the vertical velocity

307 field will gradually be generated and finally stabilized, and the stable time occurs at 5s as shown in Fig.

308 2(*b*), (*d*), (*f*) and (*h*). At 50s, the difference between the vertical velocity fields of the two equations is

309 very small as shown in Fig. 2(*g*) and (*h*).

310
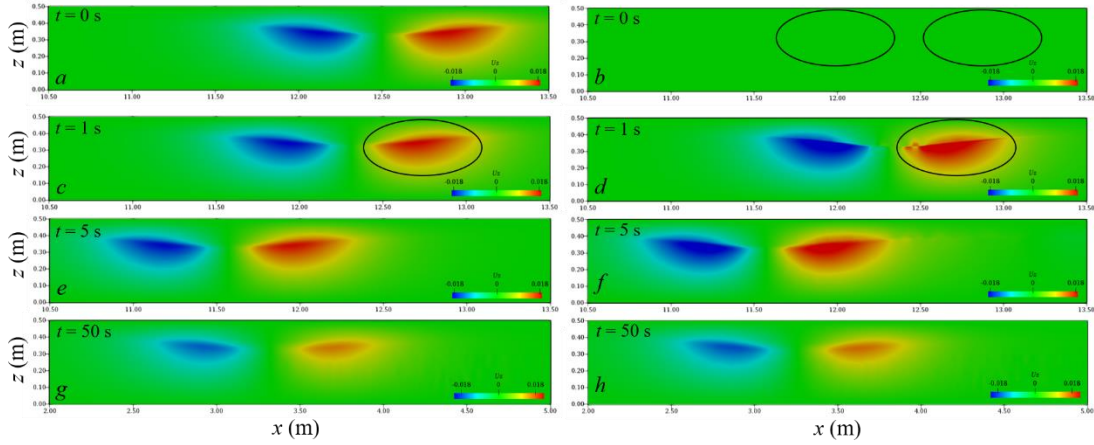
311 Figuire 2: Comparison chart of the vertical velocity component field: DJL equation (left) and eKdV equation

312 (right).

313 The ISW propagates for 10 m, and the amplitudes of the ISWs generated by the DJL equation and

314 the eKdV equation are reduced by 9.88% and 17.96%, respectively, as shown in Fig. 3. Overall, the

315 reduction in energy leads to the attenuation of the amplitude of the ISW, which in turn reduces the wave

316 speed. Except for the difference in initial fields, the grid sizes, time step, turbulence model, and other

317 features are the same. Therefore, the initial stage of ISWs generated by the eKdV equation leads to

318 excessive energy loss compared with those generated by the DJL equation. From the above analysis of

319 the velocity field, we know that the method of initializing the field with the eKdV equation requires a

320 period of movement before the jump of the velocity field develops into a field with continuous changes

321 in velocity. In addition, the DJL equation, as a fully nonlinear model, can better reflect its superiority for

322 internal waves with strong nonlinearity. Therefore, the wave generation of the subsequent numerical

323 cases in this paper adopts the method of initializing the field with the DJL equation.
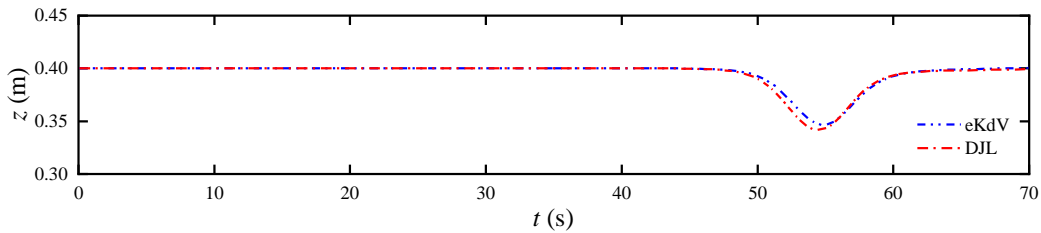
324

325 Figure 3: Time series of the interface displacement. The probe was 10 m away from the initial ISW.

3. Grid independence of the ISW simulation

These grid independence tests were performed in the horizontal and vertical directions by applying meshes of different sizes. The sizes of the mesh determined in this paper are calculated based on the amplitude of the ISW and a characteristic length determined through the integration of the wave profile (Michallet and Ivey, 1999)

$$L = \frac{1}{a} \int_{-\infty}^{\infty} \zeta(x)dx \tag{43}$$

where ζ is the isopycnal vertical displacement and a is the ISW amplitude.

To determine the appropriate mesh size, the propagation of ISWs on flat bottoms is calculated, and the numerical results are compared with the DJL theoretical solution. We set up a numerical simulation, which includes a tank that is 50 m long, 0.5 m wide and has a water depth of 0.5 m. The depths of the upper (h_1) and lower (h_2) layers are 0.1 m and 0.4 m, respectively, the densities of the upper and lower layers are 1000 kg/m^3 and 1030 kg/m^3, respectively, the location of the centre of the pycnocline (z_{pyc}) is 0.4 m, and the pycnocline thickness (d_{pyc}) is 0.05 m vertically, the ISW amplitude (a) is 0.065 m. The measuring point P is set at a position $10L$ away from the initial ISW. The sponge layer on both sides, whose length is the double wave characteristic length, has been checked to properly dissipate the reflected wave. Slip boundary conditions are applied to the bottom and both sides, while cyclic boundary conditions are assigned to the inlet and outlet boundaries. The top boundary is a rigid lid. The boundary conditions related to the density field are no-flux boundary conditions.

3.1 Grid independence in the horizontal direction

First, we analyse the grid independence in the horizontal direction, with a constant cell height of $\Delta z = a/20$ m. Fig. 4 shows the results of the comparison of the waveform and decay rate in the horizontal direction at probe P1 with the ISWFoam using a wide range of grid configurations. The results show a negligible difference in the waveform when the mesh size is less than $L/40$, so it is difficult to accurately analyse the grid independence just by the waveform. A traditional decay rate parameter is adopted, namely $\delta = (a_{probe} - a_{initial})/a_{initial}$, where $a_{initial}$ is the ISW amplitude value at the initial moment, a_{probe} is the ISW amplitude value of the probe $10L$ away from the initial ISW. Fig. 4(b) shows the relationship between the decay rate of the ISW amplitude and the grid quantity per unit length for different mesh sizes. As shown in Fig. 4(b), the decay rate of the ISW amplitude tends to be smooth as the grid number

354 per unit length increases to 160 ($\Delta x = L$/150), and then the increase in the grid quantity has a relatively

355 small effect on the decay rate. Therefore, for ISWFoam developed in this paper, we suggest that the

356 dimensions of the horizontal grid are L/150.
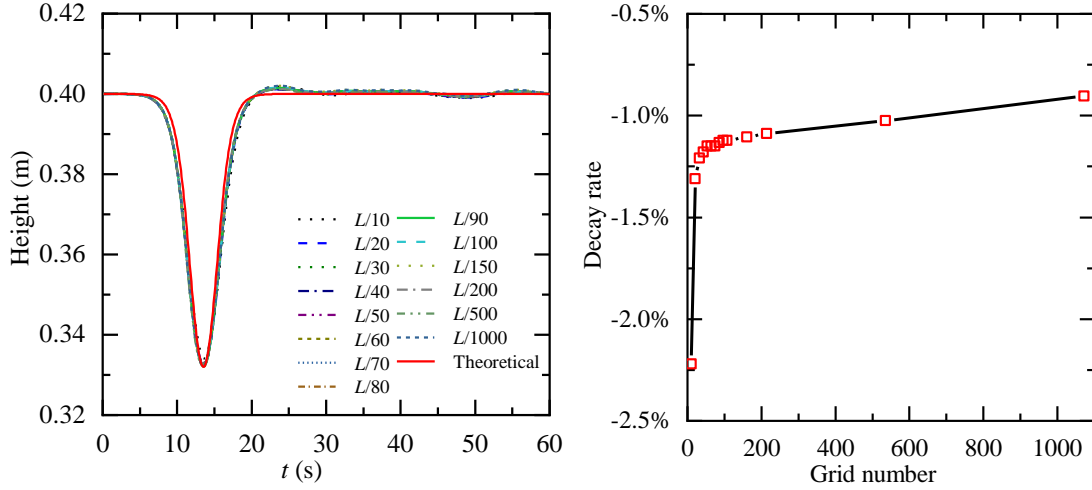
357
358 Figure 4: Grid independence in the horizontal direction at probe P1: (a) comparison of waveform and (b) decay
359 rate.

360 **3.2 Grid independence in the vertical direction**

361   Second, we analyse the grid independence in the vertical direction, with a constant cell width of Δx

362 $= L$/150 m. Fig. 5 shows the results of a comparison of the waveform and decay rate of the ISW amplitude

363 in the vertical direction at probe P1 with the ISWFoam using a wide range of grid configurations. The

364 results also show a negligible difference in the waveform when the mesh size is less than a/10, so it is

365 difficult to accurately analyse the grid independence just by the waveform. As shown in Fig. 5(b), the

366 decay rate of the ISW amplitude decreases as the grid quantity increases in a wave height range before

367 the numerical oscillation occurs. Here, we assume that the grid size with the decay rate of the ISW

368 amplitude less than one percent is the appropriate vertical grid size; namely, the vertical grid size is a/25

369 m. Therefore, for ISWFoam developed in this paper, we suggest that the dimensions of the vertical grid

370 be a/25.
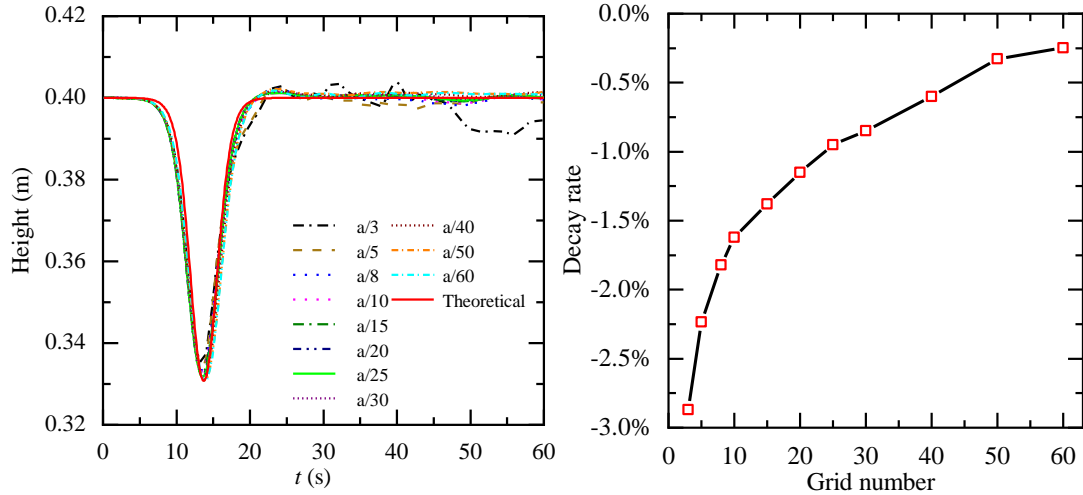
Figure 5: Grid independence analysis in the vertical direction at probe P1: (a) comparison of waveform and (b) decay rate.

Finally, for ISWFoam developed in this paper, we suggest that the dimensions of the horizontal grid are $L/150$, while the vertical grid is $a/25$.

4. Model verification and results

To verify the numerical model of the ISWs, the propagation of ISWs on a flat bottom section, submerged triangular ridge and slopes is calculated, and the numerical results are compared with the corresponding experimental results. To verify the correctness of Coriolis code implantation and reflect the role of local mesh refinement, the propagation of ISWs on a flat bottom section of actual ocean scale and a Gaussian ridge is calculated.

4.1 ISW propagating on a flat bottom section

4.1.1 Experimental data used

In this section, ISWFoam is verified by employing ISWs propagating on a flat bottom section with Case Flat_4 in the continuously stratified laboratory experiment described in Hsieh et al. (2014). The physical dimensions and ultrasonic probe locations in the experiments of Hsieh et al. (2014), as shown in Fig. 6, are adopted to establish the numerical computation domain. We set up a numerical tank of the experiment of Hsieh and co-authors, which includes a tank that is 15 m long, 0.5 m wide and has a stable water depth of 0.5 m; the fluid densities of the upper (ρ_1) and lower (ρ_2) layers are 996 kg/m^3 and 1030 kg/m^3, respectively; the ISW amplitude (a) is 0.068 m; the location of the centre of the pycnocline (z_{pyc})

391 is 0.4 m, the pycnocline thickness (d_{pyc}) is 0.04 m vertically, and the depths of the upper (h_1) and lower

392 (h_2) layers are 0.1 m and 0.4 m, respectively. The grid is uniform in the x-direction, y-direction and z-

393 direction, and the sizes are $\Delta x = 1.5 \times 10^{-2}$ m, $\Delta y = 1.5 \times 10^{-2}$ m and $\Delta z = 2.72 \times 10^{-3}$ m, respectively. The

394 sponge layer on both sides, whose length is double wave characteristic length, has been checked to

395 properly dissipate the reflected wave. Slip boundary conditions are applied to the bottom and both sides,

396 while cyclic boundary conditions are assigned to the inlet and outlet boundaries. The top boundary is a

397 rigid lid. The boundary conditions related to the density field are no-flux boundary conditions.
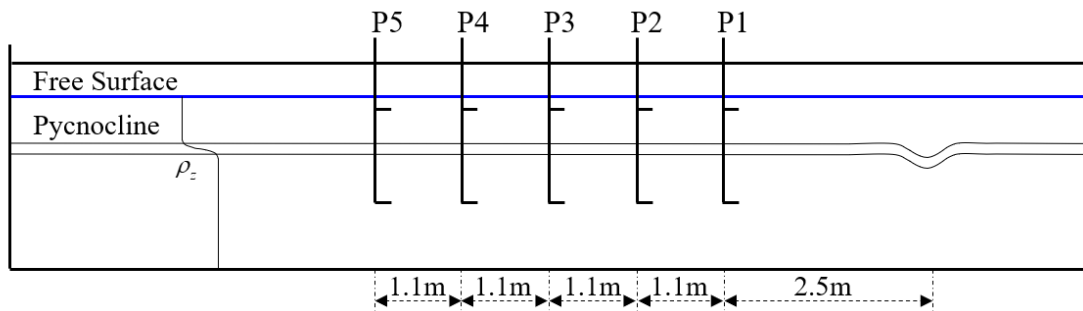
398
399 Figure 6: Schematic diagram of probe position (P1–P5) (Hsieh et al. (2014)).

4.1.2 Comparisons between the numerical and experimental results

401   Fig. 7 shows the density contours at three different times from Case Flat_4 in the laboratory

402 experiment of Hsieh and coworkers, showing the stable evolution of an ISW. The results also show the

403 realistic evolution of the thickening of the pycnocline after ISW propagation because of convection and

404 diffusion. At the same time, the propagation of the ISW is stable and unbroken.

405
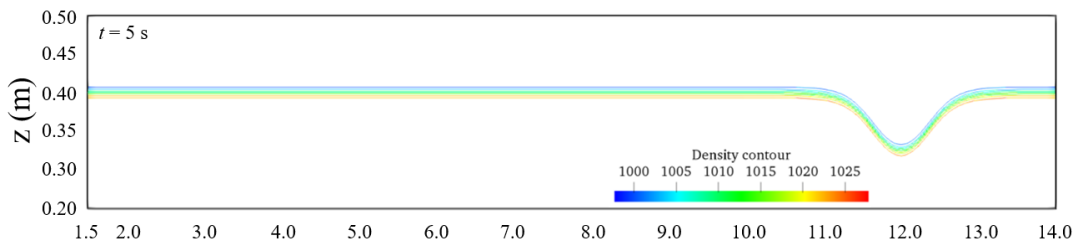
406
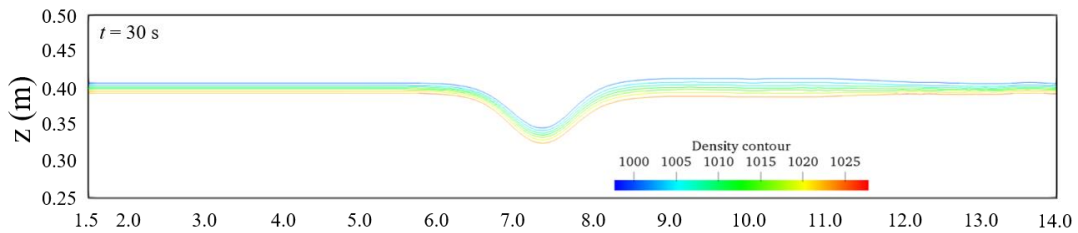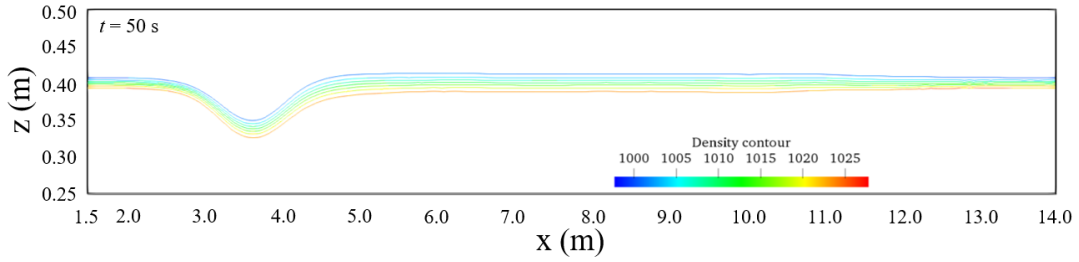
Figure 7: Density contours at different moments.

To further verify the model, the waveform is compared between the numerical simulations and the experimental measurements, and the measurement point selection is the same as the experimental setting, as shown in Fig. 6. Fig. 8 shows the comparison results between the waveform simulated by ISWFoam and the experimental results at probes P1-P5. Fig. 8 shows that the results of the numerical simulations agree with the experimental results (red circle). Notably, the laboratory wave height at the probe P1 measurement point is greater than the numerical simulation results, and the wave surface of the laboratory wave is not smooth, which is caused by the wave generation method using the gravity collapse mechanism in the laboratory. In general, the model developed in this paper can simulate the generation and evolution of ISWs in continuously stratified fluids.
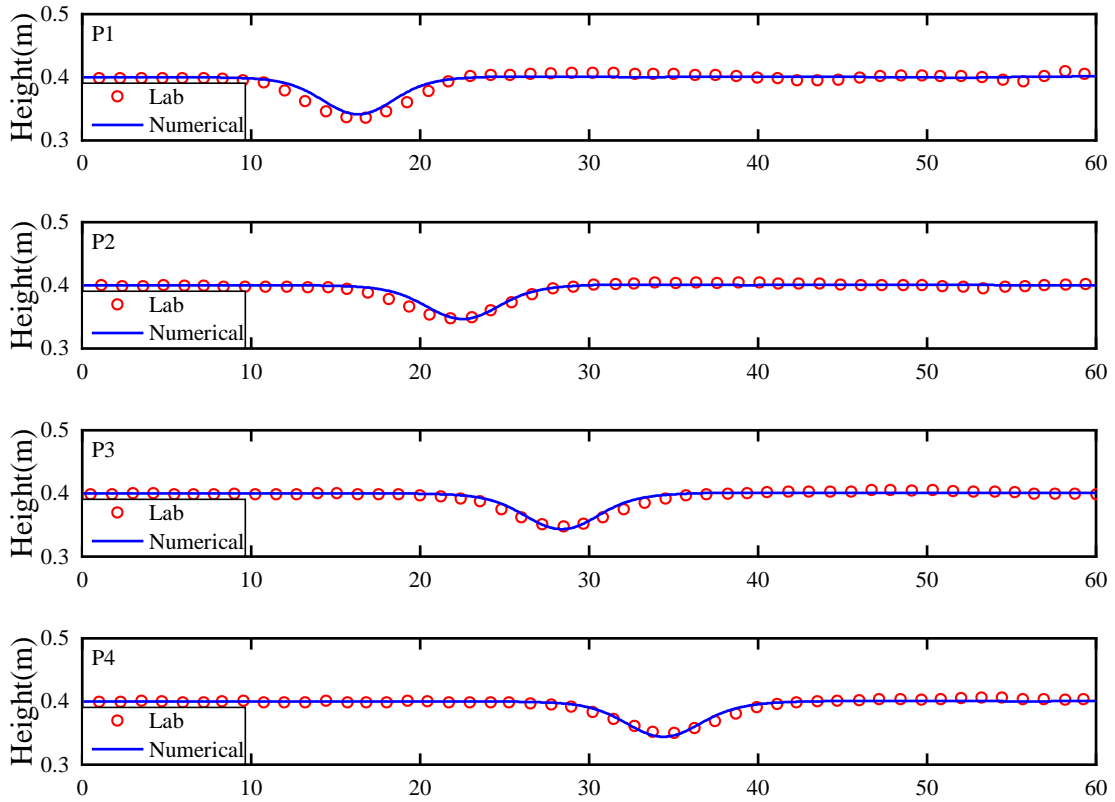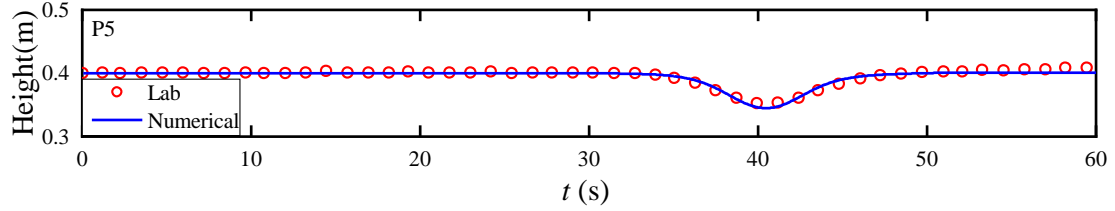
422

423   Figure 8: Comparison of the waveform between the experimental results and numerical simulation results at
424   probes P1-P5.

425   **4.2 ISW propagating over a submerged triangular ridge**

426   **4.2.1 Experimental data used**

427   In this section, the validation of the numerical model is conducted through an ISW propagating over

428   a submerged triangular ridge with the continuously stratified experiments described in Hsieh et al. (2015).

429   The laboratory tank is 12 m long and has a stable water depth of 0.5 m, with which the fluid system has

430   a finite thickness of the pycnocline. The specific experimental parameters used for validation of

431   ISWFoam include the various depths of the upper (h_1) and lower (h_2) layers; the fluid density of the upper

432   (ρ_1) and lower (ρ_2) layers of 996 kg/m^3 and 1030 kg/m^3, respectively; the ISW amplitude (α = 0.056 m);

433   the location of the centre of the pycnocline (z_{pyc} = 0.4 m); the thickness of the pycnocline (d_{pyc} = 0.04 m

434   vertically); the height of the isosceles triangular ridge (h_s = 0.30 m vertically); and the slope angle of the

435   ridge for α = 45°. The physical dimensions, and ultrasonic probe locations in the experiments of Hsieh

436   et al. (2015), as shown in Fig. 9, are adopted to establish the numerical computation domain.
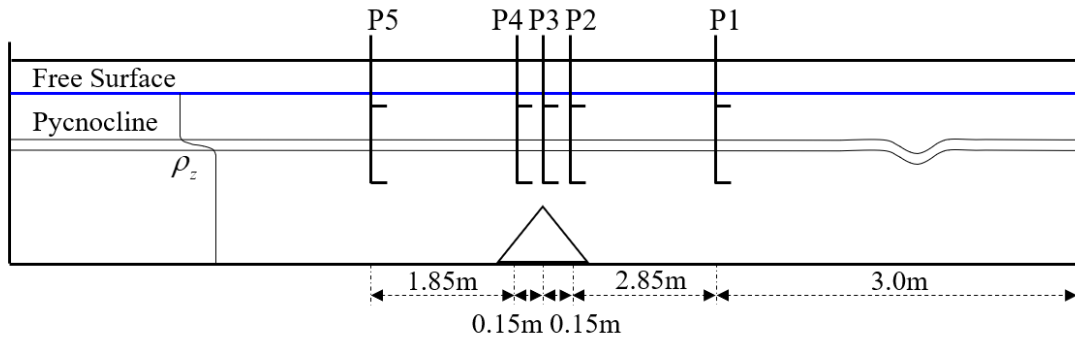
437
438   Figure 9: Schematic illustration of the laboratory setup and the locations of the probes (Hsieh et al. (2015)).

439   **4.2.2 Numerical implementation**

440   The numerical tank is designed to reproduce the experiment described in Fig. 9. The unstructured

441   grid and local mesh refinement based on the finite volume method are used to construct the computational

442   domain and discretize the governing equations. The grid is uniform in the *x*-direction, *y*-direction and *z*-

443   direction, and the sizes are $\Delta x = 2\times10^{-3}$ m, $\Delta y = 2\times10^{-3}$ m and $\Delta z = 2\times10^{-3}$ m, respectively. The precise

444   grid described triangular ridge section is $\Delta x = 2.5\times10^{-4}$ m, $\Delta y = 2.5\times10^{-4}$ m and $\Delta z = 2.5\times10^{-4}$ m at the

445   slope, as shown in Fig. 10. The sponge layer on both sides, whose length is double the wave characteristic

446   length defined through integration of the wave profile in Section 3 for this case, has been checked to

447   absorb the reflected wave well. A rigid wall conditions is applied to both sides, while the slip and slip

448   conditions are assigned to the bottom and the surface of the submerged ridge boundaries, respectively.

449   The top boundary is a rigid lid. The inlet and outlet boundaries adopt cyclic boundary condition. The

450   boundary conditions related to the density field are no-flux boundary conditions.
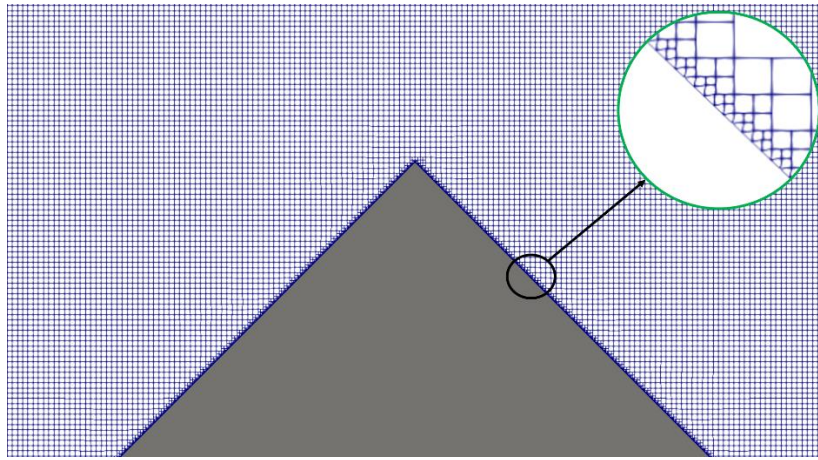
451
452   Fig. 10. Schematic of the mesh

453   **4.2.3 Comparisons between the numerical and experimental results**

454   Fig. 11 shows the comparison results between the waveform calculated by ISWFoam and the

455   experimental results at probes P1-P5. In each subplot, the results of the numerical simulations (blue line)

456   are found to be in good agreement with the experimental results (red circle). From Fig. 11 (a), the

457   numerical simulation result of the probe P1 measurement after 20 s is different from the experimental

458   results, which is caused by the different ISW generation methods. For the experimental results, the first

459   large leading ISW is formed via the gravity collapse mechanism, which is trailed by a train of small-

460   amplitude mode-one waves that is generated due to shear instabilities. However, the initialization method

461   used to generate an initial ISW for the numerical simulation in this paper is more stable than the gravity

462   collapse mechanism, so the rear part of the ISW is relatively flat compared to the experimental results

463   for probe P1. In Fig. 11, the waveform of the ISW gradually evolves towards a flat waveform due to the

464   interaction between the ISW and the ridge. In general, the model developed in this paper can simulate

465   the interaction between ISWs and structures.
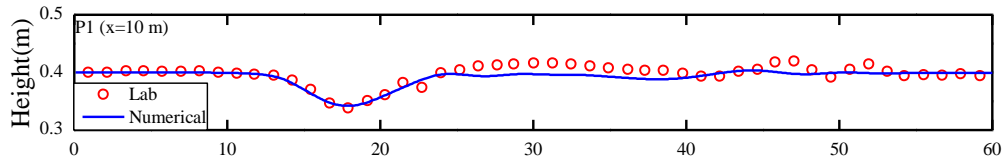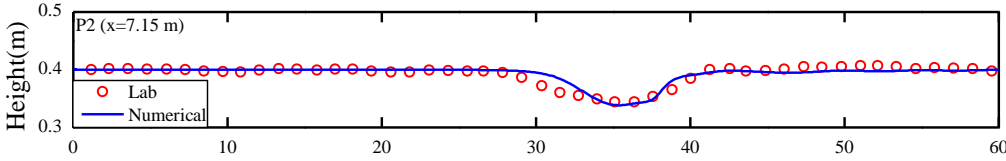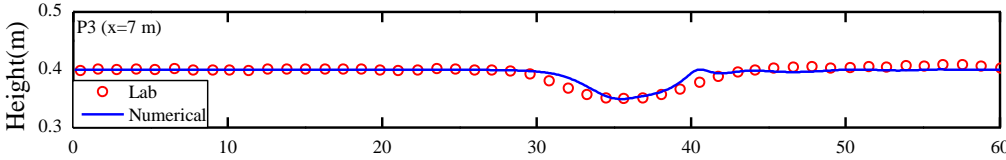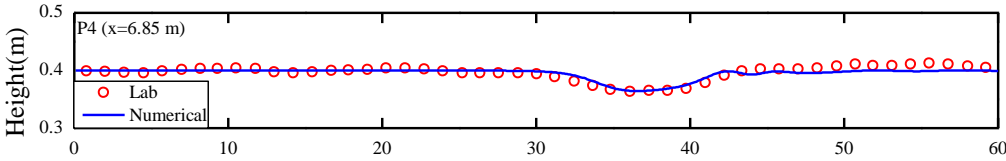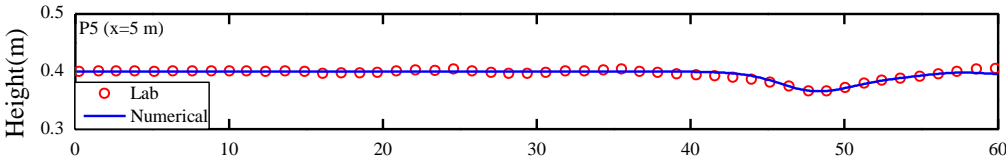
Figure 11: Comparison of the waveform between the experimental results in Hsieh et al. (2015) and numerical simulation results at probes P1-P5.

4.3 ISW propagating on a slope

To verify the ability and accuracy of simulating the ISW breaking of the numerical model, two continuously stratified laboratory experiments (12 and 15) of Michallet and Ivey. (1999) are chosen for the simulation in this section. The experimental setup is represented schematically in Fig. 12. We set up a numerical tank of the experiment of Michallet and Ivey. (1999), which includes a tank is L= 4.2 m long, 0.25 m wide and has a water depth of 0.15 m. The layer thickness ratio (h/H) varies from 0.60~0.91. A linear slope s = 0.214 starts at 0.7 m from the right end of the tank for experiments 12 and 15. The grid is uniform in the x-direction, y-direction and z-direction, and the sizes are Δx = 2.5×10^{-3} m, Δy = 2.5×10^{-3} m and Δz = 1.25×10^{-3} m, respectively. The precise grid describing the slope section is $\Delta x = \Delta y$ = 6.25×10^{-4} m and Δz = 3.125×10^{-4} m at the slope.
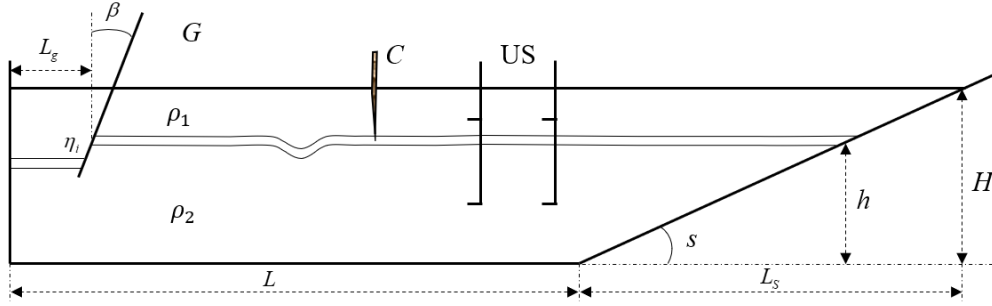
483

484 Figure 12: Schematic diagram of the laboratory setup. "C" and "US" represent the experimental device at probes.

485 The sponge layer on the left side, whose length is the double wave characteristic length, is checked

486 to properly dissipate the reflected wave. Slip boundary conditions are applied to the bottom and both

487 sides, while slip boundary conditions are assigned to the top boundaries. The boundary conditions related

488 to the density field are no-flux boundary conditions.

489 The vertical profile of the initial density is given by a hyperbolic tangent function profile

490
$$\overline{\rho}(z) = \rho_1 + \frac{\Delta\rho}{2}\left\{1+\tanh\left[\frac{-\left(z-z_{pyc}\right)}{d_{pyc}}\right]\right\}$$
(44)

491 where z is the vertical position, $\rho_1 = 1\times10^3$ kg/m^3 is the base density field, $\Delta\rho$ is the change in the density,

492 z_{pyc} is the location of the centre of the pycnocline, and d_{pyc} is the thickness of the pycnocline.

493 **4.3.1 Case one and results**

494 The first case of model verification is experiment 12 of Michallet and Ivey. (1999) in this section.

495 The layer thickness ratio (h/H) is 0.84, and the density change ($\Delta\rho$) value is 14 kg/m^3. Fig. 13 presents

496 the time series for the interface displacement (ζ) for experiment 12 of Michallet and Ivey. (1999). The

497 results indicate reasonably good agreement between the time series of the simulated interface

498 displacement and that of the laboratory results. The first trough centred around $t = 25$ s represents the

499 incident ISW propagating the probe 99.8 cm away from the start of the slope. The second trough centred

500 at approximately $t = 87$ s represents the reflected ISW at the generation side, which has a smaller

501 amplitude and a longer wavelength than the incident ISW as the energy in the wave decreases. As shown

502 in Fig. 13, the smooth waveform of the incident ISW of the numerical simulation indicates that the

503 initialization method of wave generation in this paper is more stable than the experiment.
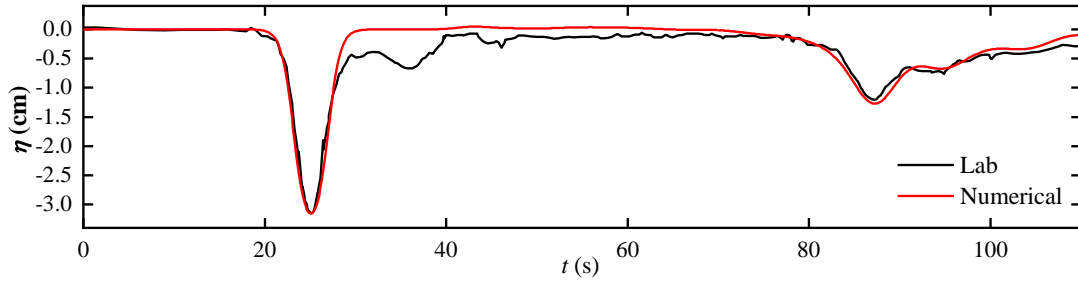
504
505   Figure 13: Time series of the interface displacement. The probe was 99.8 cm away from the start of the slope.

506   Fig. 14 shows a comparison of ISWFoam results and the experimental observations of the velocity

507   field associated with the ISW run-up process along the slope. The model effectively reproduces

508   laboratory tests, such as the intensity and direction of the velocity field, the location of the vortices, and

509   the occurrence of boundary-layer separation beneath the ISW. Therefore, the model developed in this

510   paper can reflect the ISW breaking phenomenon during the propagation of ISWs along the slope.
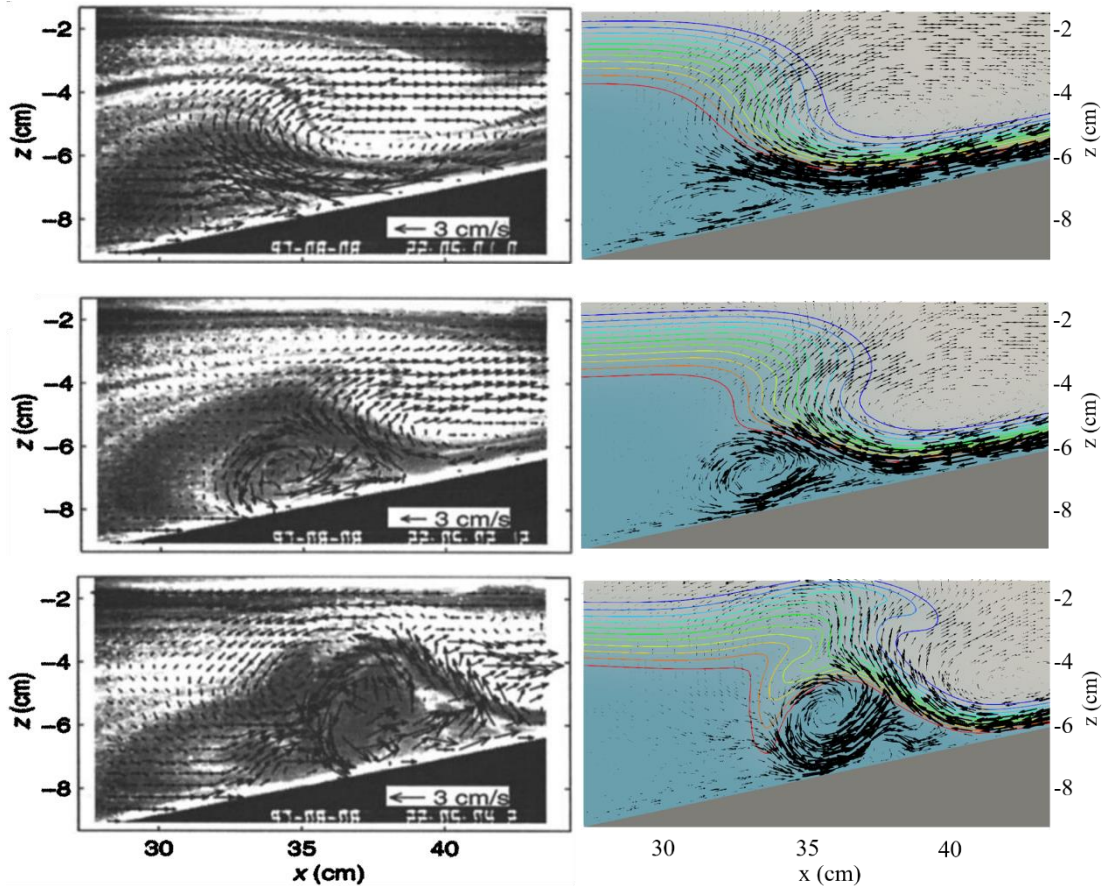
513
514   Figure 14: Comparison of the velocity field between the experimental observation results in Michallet and Ivey.
515   (1999) (left) and numerical simulation results (right).

516   **4.3.2 Case two and results**

517   Another laboratory experiment that more clearly shows the ISW breaking phenomenon from

518   Experiment 15 of Michallet and Ivey. (1999) is used to verify the numerical model presented in this paper,

519   and the corresponding numerical case is set corresponding to it. The layer thickness ratio (h/H) is 0.77,

520   and the density change ($\Delta\rho$) value is 47 kg/m^3. The wave amplitude and phase velocity at the slope

521   calculated by ISWFoam are 2.71×10^{-3} m and 10.83×10^{-1} m/s, which fit well with the experimental results

522   of 2.7×10^{-3} m and 10.8×10^{-1} m/s.

523   Fig. 15 shows the results of the numerical simulations of the ISWs propagating along the slope and

524   wave breaking using ISWFoam. As the ISW propagates to the slope, according to the conservation of

525   mass, the upper fluid forward and the downward velocity of the lower fluid increasing along the slope

526   results in the formation of a thin boundary layer, as shown in Fig. 15(a), (b), and (c). At the same time,

527   the amplitude of the ISW increases, and the rear of the ISW gradually becomes very steep but does not

528   overturn. With the development of the ISW, the rear waveform of the ISW cannot maintain its stability

529   and overturns forward, resulting in wave breaking, as shown in Fig. 15(d). After wave breaking occurs,

530   the denser lower layer flow accelerates into the less dense upper layer flow, forming a mixture region, as

531   shown in Fig. 15(e). After the lower layer flow is drawn downward from beneath the ISW, a mixing

532   region comprised of vortices is pushed upwards along the slope while the leading waveform is reflected,

533   as shown in Fig. 15(f), (g), and (h). Fig. 15(i), (j) shows the falling process of ISWs. From the perspective

534   of the entire process of wave breaking, the steepening of the rear waveform in this case is the main reason

535   for wave breaking.
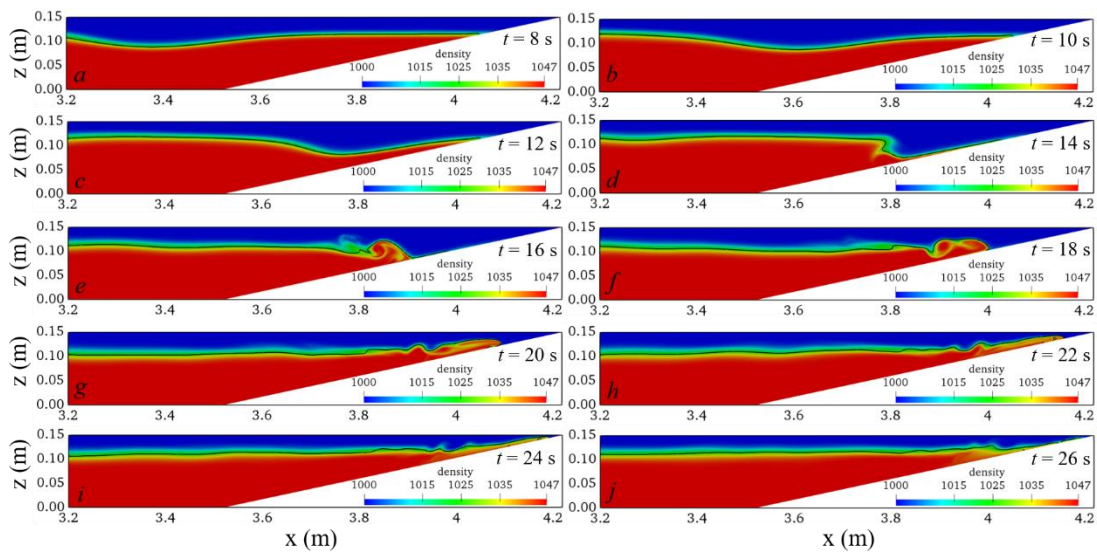
536
537   Figure 15: Temporal and spatial variations in the ISWs breaking calculated using ISWFoam (the black line
538   represents the waveform).

539   For comparison with the flow visualization image of the experiment, a specified thickness of the

pycnocline is presented, and the pycnocline ranges from 1003 kg/m^3 to 1045 kg/m^3 with dark colours as shown in Fig. 16.

Fig. 16 compares the ISWFoam results and the experimental results of Michallet and Ivey. (1999) before, during, and after ISW breaking. The results indicate that some main features of the laboratory tests are reasonably well reproduced by ISWFoam, such as the profile of ISW, the location of the wave breaking point, ISW arrival time, and spatial and temporal changes in the mixture region. Therefore, the model developed in this paper can accurately simulate the ISW breaking phenomenon during the propagation of ISWs along the slope.
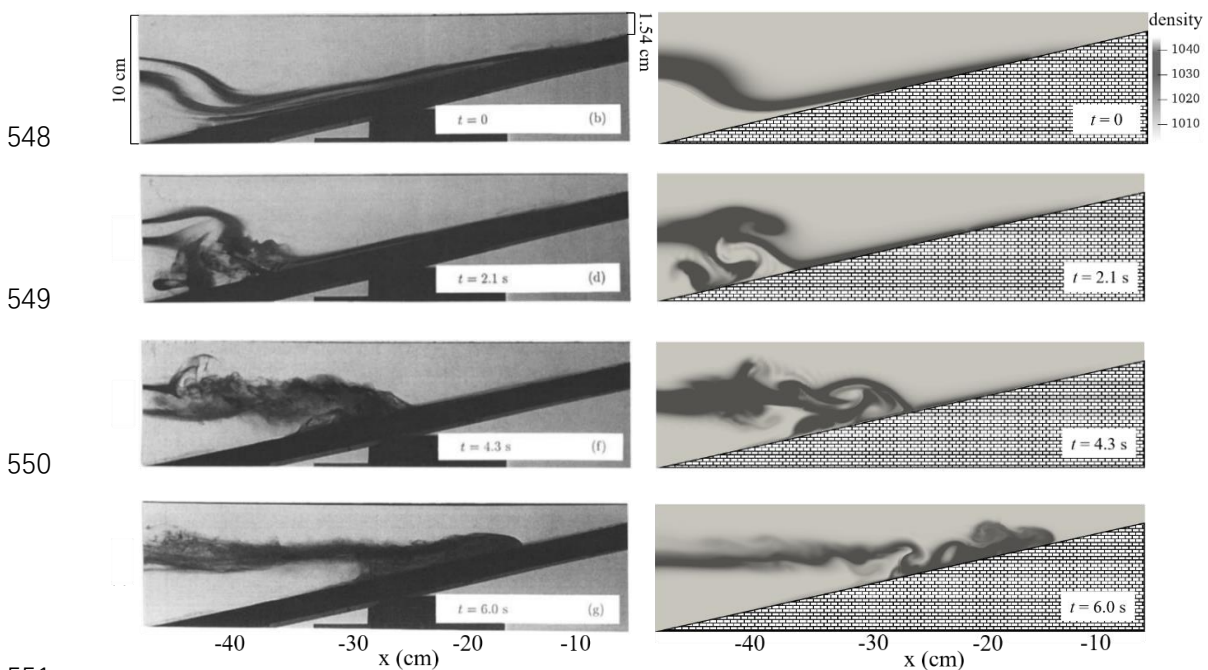
Figure 16: Comparison of the density fields between the experimental observation results in Michallet and Ivey. (1999) (left) and the numerical simulation results (right).

5. Simulation examples at the field scale

The ISWFoam model developed in the present paper can be used as a tool to investigate the interaction between ISWs and complex structures and topography. In this section, two numerical examples are presented to show the capability of ISWFoam on field scale simulation.

5.1 ISW propagating over a 3D Gaussian ridge

We designed a case of an ISW propagating over a 3D Gaussian ridge. The 3D Gaussian ridge is obtained by rotating a 2D Gaussian ridge

561 $$z = ae^{-(x/l)^2} \qquad (45)$$

562 where a is the ridge amplitude, and l is the standard deviation. With $a = 100$ m and $l = 10$, we can obtain

563 a 2D Gaussian ridge with a height of 100 m and a bottom width of 40 m. Subsequently, the 3D Gaussian

564 ridge can be obtained after a vertical rotation of 180 degrees.

565 We set up a 3D numerical tank, which includes a tank that is 3 km long, 400 m wide (y-direction

566 from -200 m to 200 m) and has a water depth of 120 m. The depths of the upper (h_1) and lower (h_2) layers

567 are 20 m and 100 m, respectively, the densities of the upper and lower layers are 1000 kg/m^3 and 1030

568 kg/m^3, respectively, the location of the centre of the pycnocline (z_{pyc}) is 100 m, and the pycnocline

569 thickness (d_{pyc}) is 1.5 m vertically, the ISW amplitude (a) is 20 m. The Gaussian ridge is located at 800

570 m horizontally. The grid is gradually changed from $\Delta x = 20$ m to $\Delta x = 2.5$ m in the x-direction, the grids

571 in the y-direction are uniform with a constant cell width of $\Delta y = 2.5$ m, and the grids in the z-direction

572 are non-uniform, with a minimum cell height of $\Delta z = 1$ m near the interface of the ISW. The precise grid

573 described the 3D Gaussian ridge section as $\Delta x = 3.9 \times 10^{-2}$ m, $\Delta y = 3.9 \times 10^{-2}$ m and $\Delta z = 1.56 \times 10^{-2}$ m, as

574 shown in Fig 17. The sponge layer on both sides, whose length is the double wave characteristic length,

575 has been checked to properly dissipate the reflected wave. Slip boundary conditions are applied to the

576 bottom and both sides, while cyclic boundary conditions are assigned to the inlet and outlet boundaries.

577 The top boundary is a rigid lid. The boundary conditions related to the density field are no-flux boundary

578 conditions.
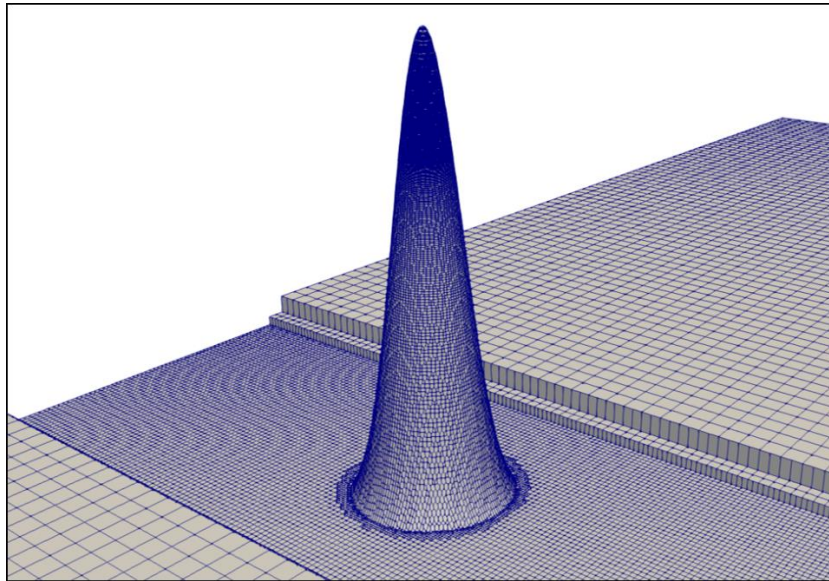
579

580 Figure 17: Schematic of the local refinement of the grid.

581 Fig. 18. shows the temporal and spatial variations in the ISWs propagating over a 3D Gaussian

582   ridge. The ISW reaches the Gaussian ridge, causing the wave surface in front of the ridge to decrease,

583   and the wave surface behind the ridge to climb up the ridge, as shown in Fig. 18(*a*). Due to being

584   obstructed by the Gaussian ridge, flow around a ridge and wave surface uplift are generated on both sides

585   of the Gaussian ridge (perpendicular to the direction of wave propagation), as shown in Fig. 18(*b*). As

586   the ISW propagated over the Gaussian ridge, the wave surface climbed along the ridge, and at the same

587   time, low velocity was generated behind the ridge, as shown in Fig. 18(*c*). Since the top of the ridge is in

588   the pycnocline, there will be a low velocity area behind the ridge for a period of time after the ISW passes,

589   as shown in Fig. 18(*d*). In general, the ISWFoam model with unstructured grids and local mesh

590   refinement can simulate the interaction between ISWs and complex structures and topography at the field

591   scale.
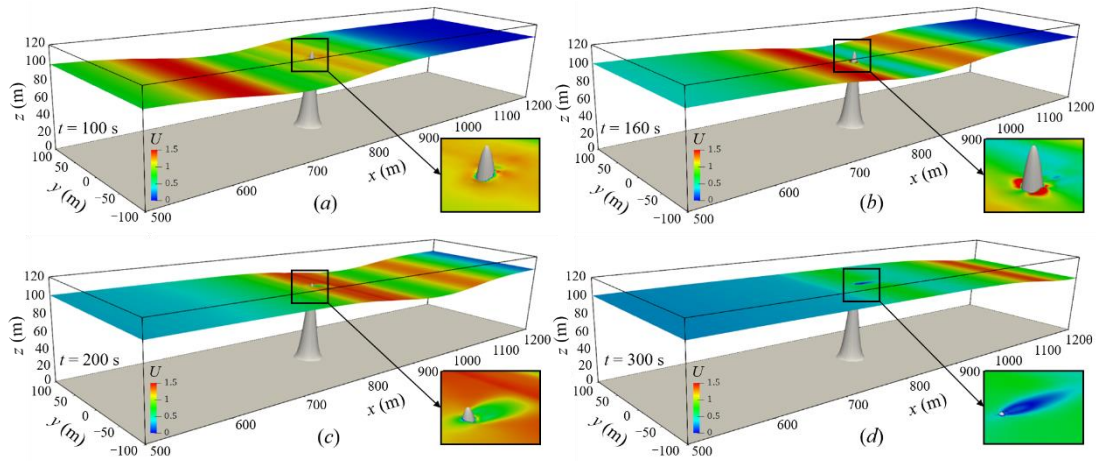
592

593   Figure 18: Temporal and spatial variation in the ISWs propagating over a 3D Gaussian ridge.

594   **5.2 ISW propagating over a hyperbolic tangent terrain**

595   The propagation of ISWs to the shore is bound to be affected by the continental shelf, and

596   shallow water evolution phenomena such as nonlinear evolution, breaking phenomenon and

597   waveform inversion occur on the undulating continental shelf. For simplicity, this section simplifies

598   the continental shelf into a hyperbolic tangent terrain, the terrain profile formula is as follows (Lamb,

599   2002)

600     $$z = \frac{a_T}{2}\left(1 + \tanh\left(\frac{x}{L}\right)\right) \tag{46}$$

601   where a_T is the ridge amplitude, which is 60 m, and *l* is the width of the continental shelf change area,

602   which is 200 m, and x and z are the horizontal and vertical coordinate positions, respectively.

603   We set up a 3D numerical tank, which includes a tank that is 7.5 km long, 200 m wide (y-direction

604   from -100 m to 100 m) and has a water depth of 100 m (z-direction from 0 m to 100 m). The depths of

605   the upper (h_1) and lower (h_2) layers are 20 m and 80 m in the deep water, respectively, and the depths of

606   the upper (h_1) and lower (h_2) layers are both 20 m in the shallow water. The densities of the upper and

607   lower layers are 1000 kg/m^3 and 1012 kg/m^3, respectively, and the pycnocline thickness (d_{pyc}) is 2 m, the

608   location of the pycnocline (z_{pyc}) center is at 80 m, the ISW amplitude (a) is 20 m. The starting point of

609   the hyperbolic tangent terrain is located at 0 m horizontally, and the top of the terrain is 40 m underwater.

610   Therefore, ISWs will gradually propagate from deep water area with a water depth of 100 m to shallow

611   water area with a water depth of 40 m. The horizontal grid is gradually changed from 40 m at the inlet to

612   4 m in the study area, and then from the study area to 60 m at the outlet, the grid is uniform in the y-

613   direction and z-direction, which are 4 m and 1 m. The hyperbolic tangent terrain is characterized by 4-

614   level local mesh refinement, and the minimum grid size is 5 cm, as shown in Fig 19. The sponge layer

615   on both sides, whose length is the double wave characteristic length, has been checked to properly

616   dissipate the reflected wave. Cyclic boundary conditions are assigned to the inlet, outlet and both sides,

617   while the slip and non-slip conditions are assigned to the bottom and the shelf topography. The top

618   boundary is a rigid lid. The boundary conditions related to the density field are no-flux boundary

619   conditions.
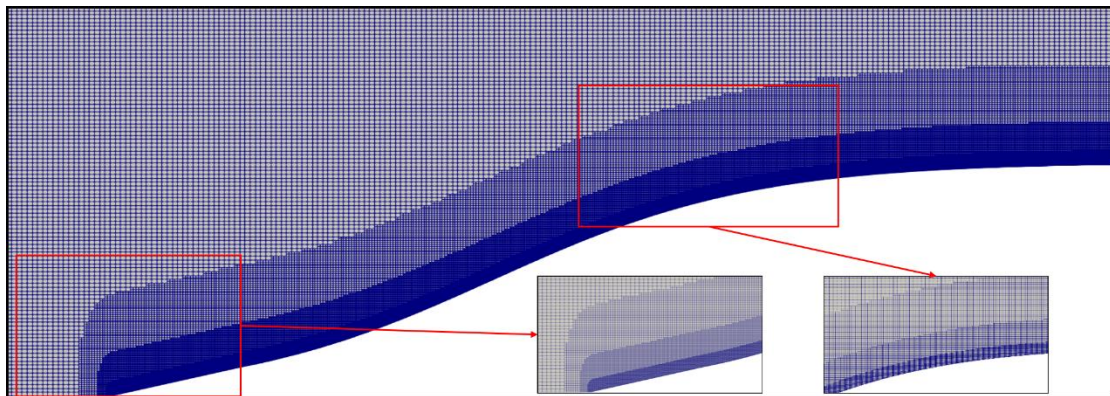
621   Figure 19: Schematic of the local refinement of the grid.

622   Fig. 20. shows the waveform and velocity field when the ISW passes through the hyperbolic tangent

623   terrain. From Fig. 20, it can be seen that the ISW breaks and has a significant waveform inversion when

624   propagating from deep water of 100 m to shallow water of 40 m. As the ISWs propagate to the continental

625   shelf, the water depth gradually becomes shallower, and the thickness of the lower fluid gradually

decreases as shown in Fig. 2-20(*a*). Due to the presence of the continental slope, the nonlinearity of the ISWs becomes stronger, and the trough velocity of the ISWs is significantly lower, which causes the waveform at the rear of the ISW to become steep, as shown in Fig. 2-20(*b*). At the same time, the front waveform of the ISW gradually becomes flat and parallel to the shelf topography. As the waveform at the rear of the ISW becomes steeper and loses balance, the waveform at the rear of the ISW rolls forward, leading to the occurrence of ISW breaking phenomenon, as shown in Fig. 2-20(*c*). It is worth noting that the ISW breaking occurs at the rear of the ISW, while the front waveform does not break, but transforms into another form of wave (referred to as the head wave), and continues to propagate steadily along the continental shelf. The breaking of ISWs causes severe disturbances in the water, and excite a series of secondary waves at the tail of the head wave, represented by elevation ISWs (as shown in Fig. 2-20(*d*), (*e*), (*f*)), and then elevation ISWs propagate forward steadily in shallow water (as shown in Fig. 2-20(*g*), (*h*), (*i*)). The shelf slope of the case in this section is the same as the shelf slope of s8_c1c case studied by Lamb and Xiao (2014), both of which are 0.1. The research results of Lamb and Xiao (2014) show that waveform inversion of a depression ISW will occur at this shelf slope, and a series of elevation ISWs will be generated and propagate stably in shallow water. The simulated results have good agreement with that of Lamb and Xiao (2014).
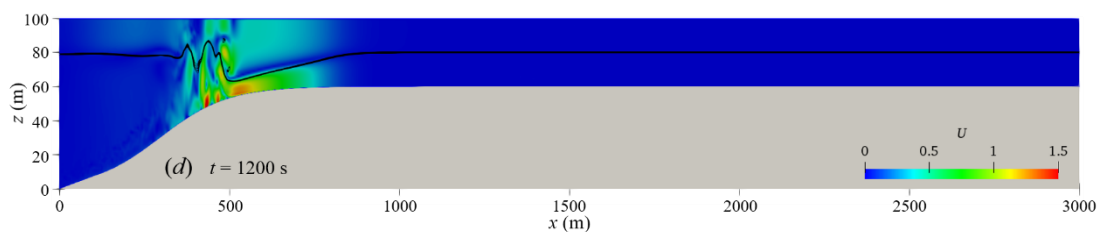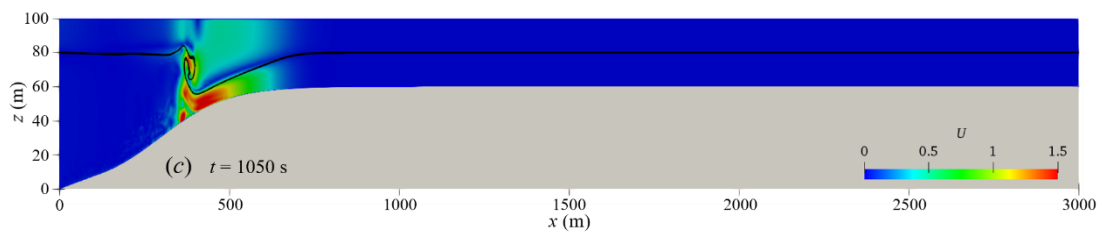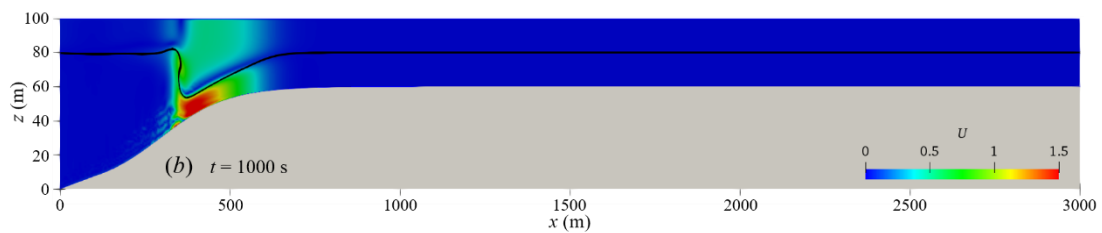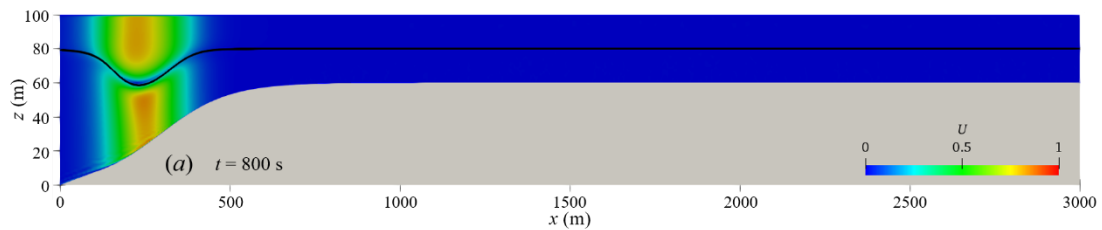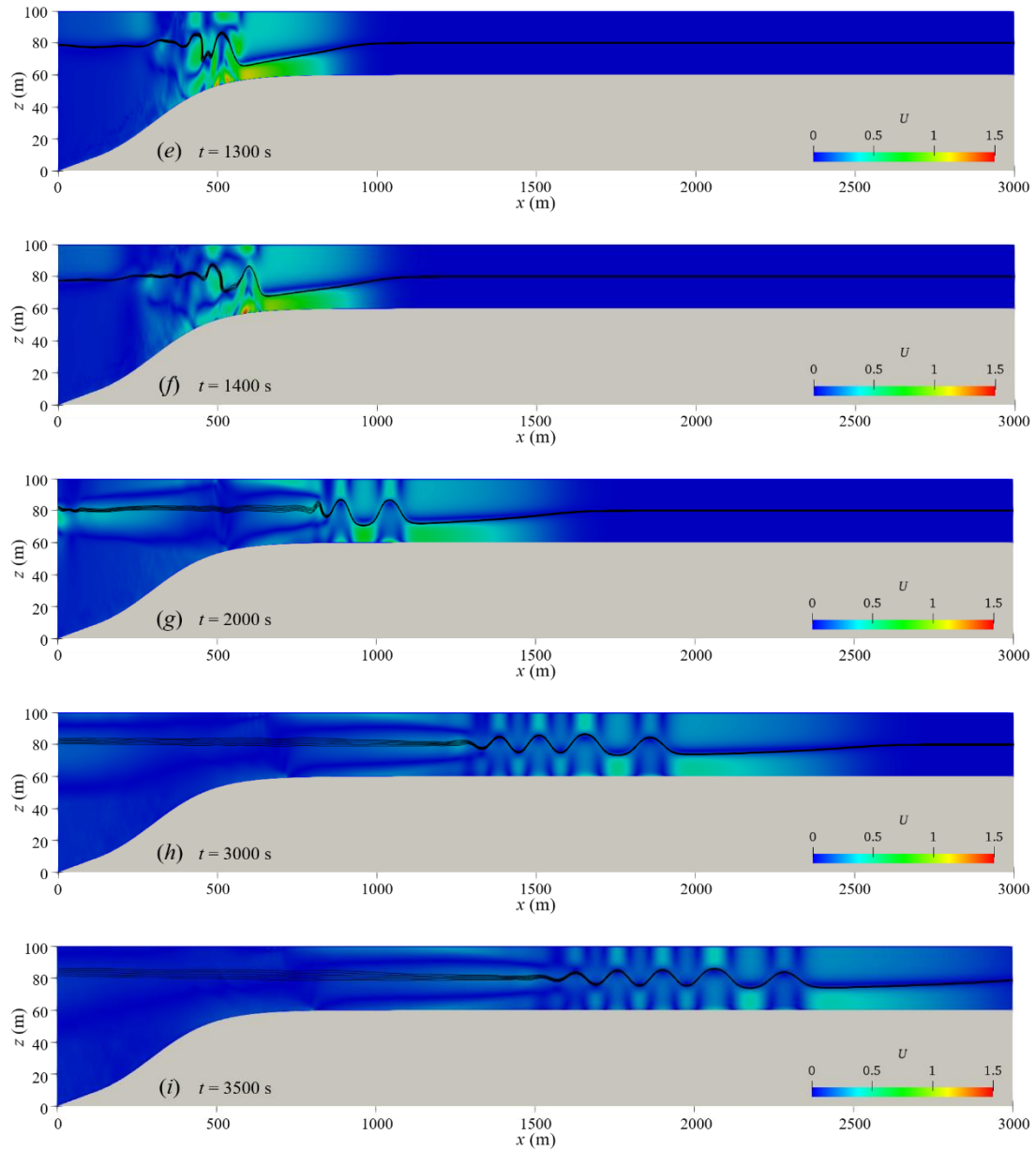
Figure 20: Velocity field diagram of ISW propagation (the black solid line is the iso-density contours).

The vortex structure has an important influence on the material transport at the bottom of the shelf, so it is very necessary to study the vortex structure when the ISW breaks. Fig. 2-21 shows the vorticity field of the ISW at the breaking stage. With the occurrence of ISW breaking, a significant counterclockwise vortex structure is generated below the waveform at the rear of the ISW, as shown in Fig. 2-21(*a*). With the propagation of the head wave, the vortex climbs along the shelf, and the vortex continues to develop horizontally and vertically during the upward climb, and the vertical scale is about 1/3 of the local water depth (as shown in Fig. 2-20(*b*), (*c*)). As the vortex structure continues to climb, the vorticity decays, and the vortex structure gradually disappears, as shown in Fig. 2-21(*d*), (*e*). Combined with the velocity field in Fig. 2-20, it can be seen that the vorticity before and after the ISW breaks is the largest, and the vortex structure is the most obvious. As the wave train of elevation ISWs

662 propagates steadily, the vortex structure climbs up the shelf and gradually disappears.
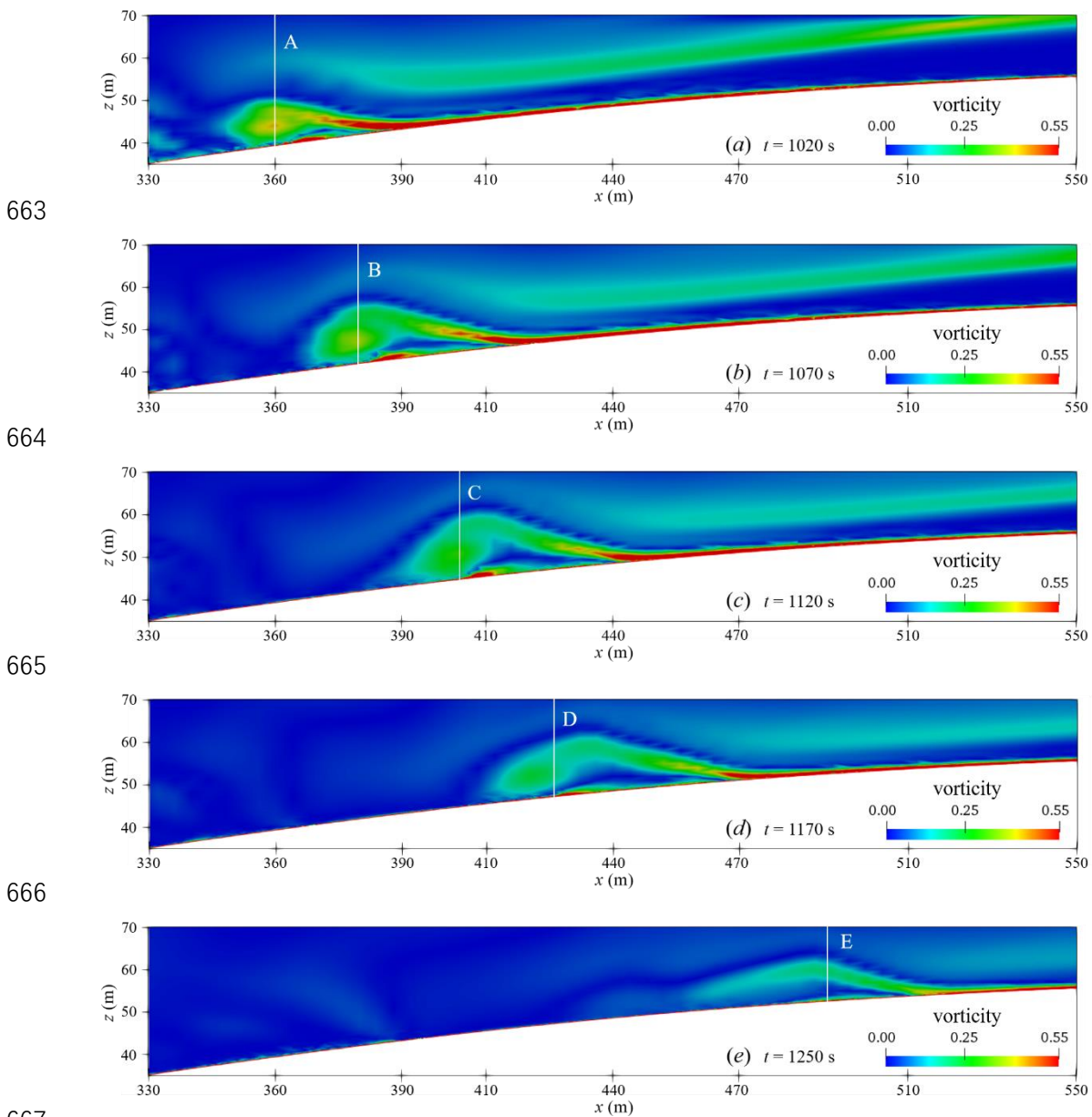
Figure 21: Vorticity field (A-E represents transverse section)

669   In order to analyze the vortex of the three-dimensional structure, Fig. 2-22 shows the vorticity

670 field diagram on the transverse section, and the position of the transverse section corresponds to the

671 marked section in Fig. 2-21. It can be seen from Fig. 2-22 that the vortex also evolves in the

672 transverse section. Obviously, the bottom vortex structure generated by ISW breaking shows three-

673 dimensional non-uniform features.

674

675

676

677

678
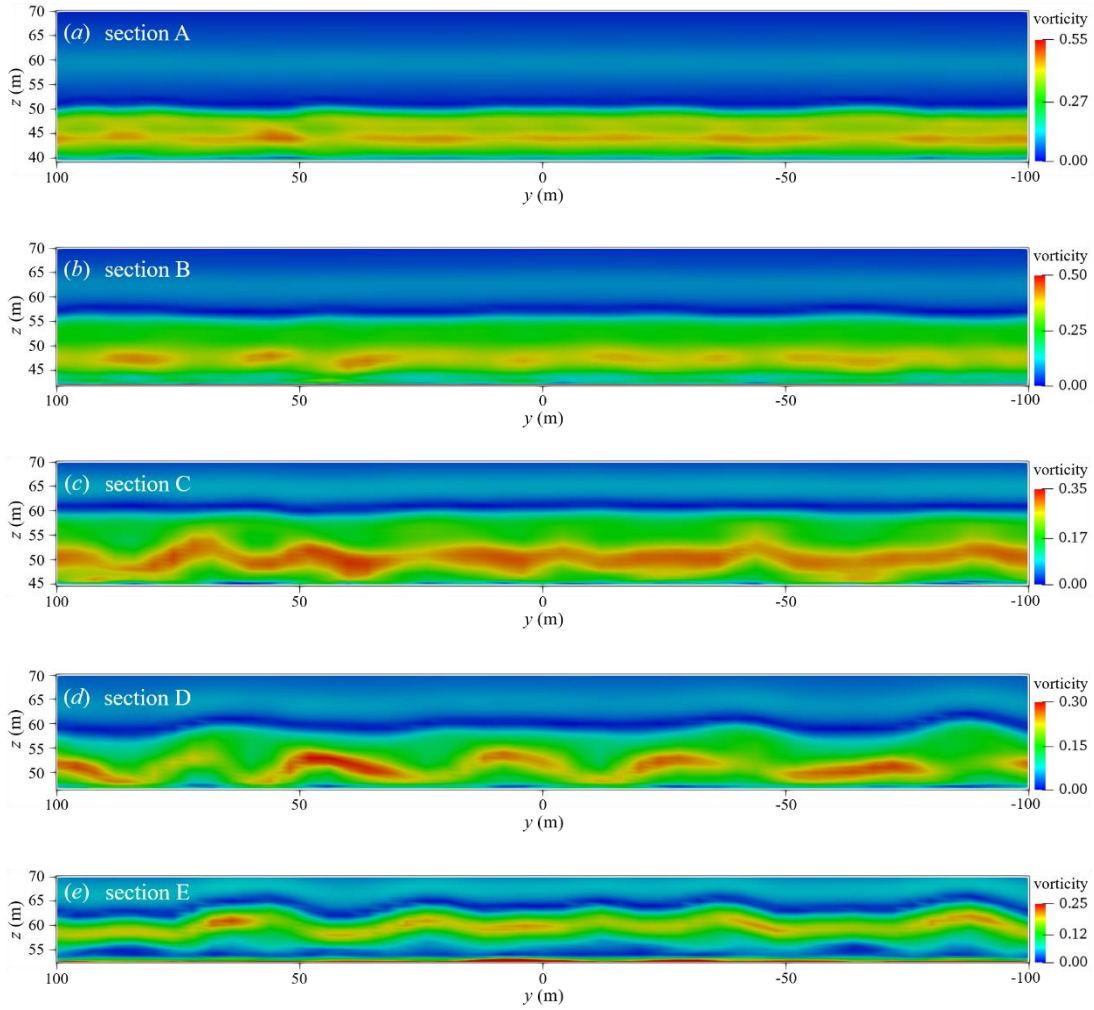
679 Figure 22: Vorticity field of transverse section.

680   The velocity vector field of the head wave and the wave train of elevation ISWs in the shallow

681 water area are shown in Figure 2-23. The head wave generated by the breaking of the ISW loses the

682 original wave shape of the ISW, the wave height becomes smaller, the wavelength becomes longer,

683 and the velocity field is still in the form of upper layer forward and lower layer backward (as shown

684 in Fig. 2-23(*a*), (*b*)). In Fig. 2-23(*c*), (*d*), the velocity field and waveform of the entire wave train

685 following the head wave are stable, and the velocity field of each wave is backwards in the upper

686 layer and forwards in the lower layer, and the wavelength gradually becomes longer as the wave

687 train propagates. As the wave train propagates in shallow water, there is a large vorticity in the crest

688 and trough areas of each wave, and it propagates forward steadily as the wave train propagates, as

689 shown in Fig. 2-24. Generally, the waveform inversion and breaking phenomenon of ISWs is well

690 indicated, and the propagation and evolution of the wave train generated by waveform inversion is

691 also accurately described through ISWFoam simulation.
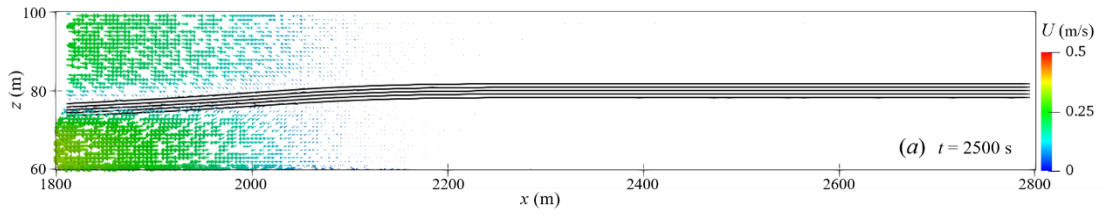
692
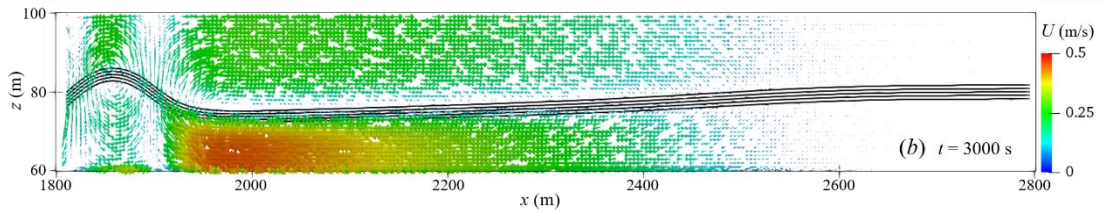
693
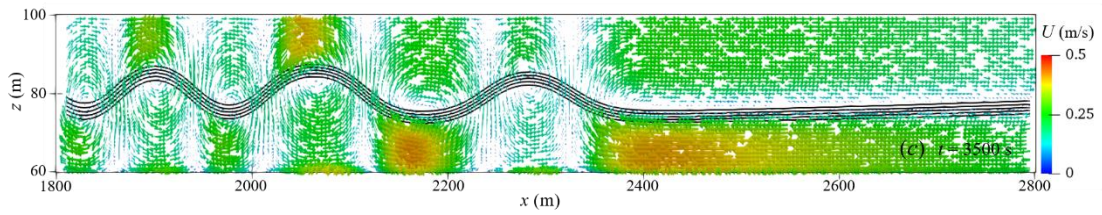
694
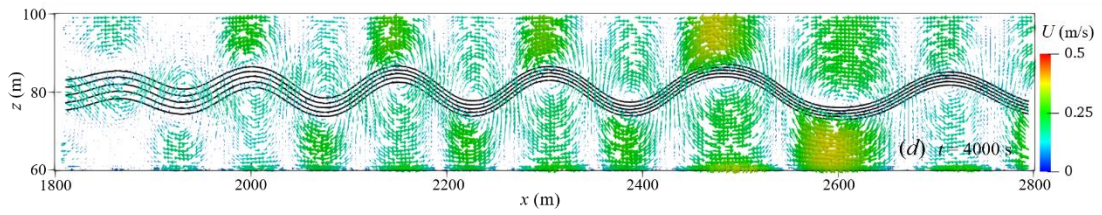
695

696   Figure 23: Velocity vector field of wave train in shallow water area.

697

698

699

700
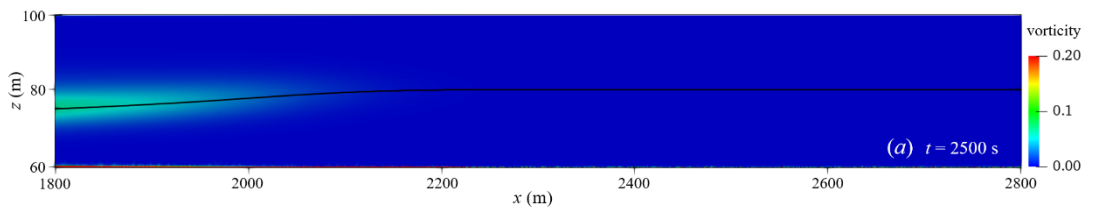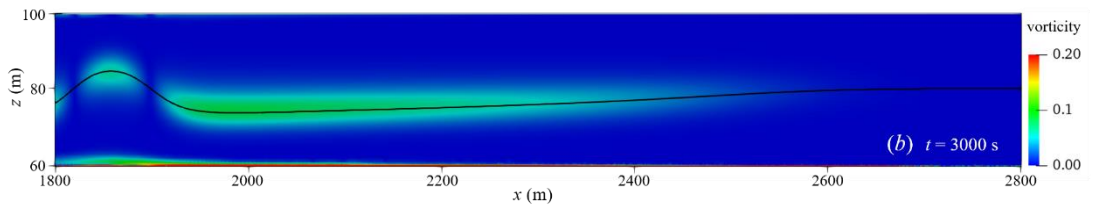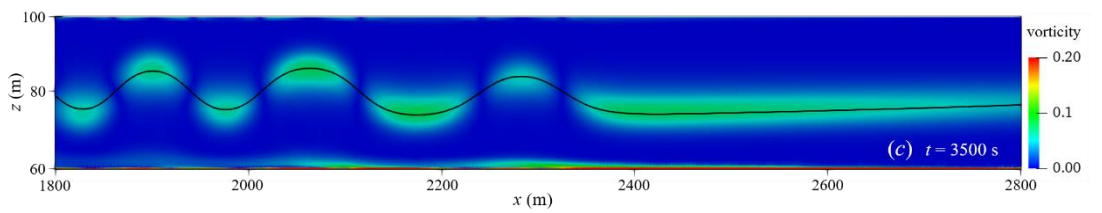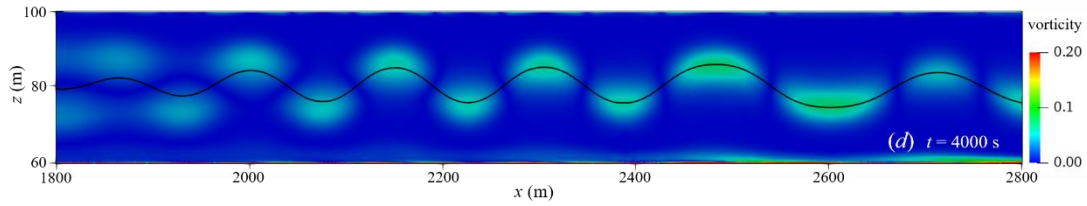
701 Figure 24: Vorticity field of wave train in shallow water (the black solid line is the waveform).

702 **6. Conclusions**

703 In this paper, a numerical model referred to as ISWFoam with a modified *k-ω SST* model,

704 established by combining the density transport equation with a fully three-dimensional (3D) Navier-

705 Stokes equation, is developed to simulate ISWs in continuously stratified, incompressible, viscous fluids

706 based on the finite volume method with unstructured grids and local mesh refinement of OpenFOAM.

707 ISWFoam provides two initial wave generation methods to generate an ISW in continuously stratified

708 fluids, including solving the weakly nonlinear models of the eKdV equation and the fully nonlinear

709 models of the DJL equation. The verification process presents several applications, such as ISWs

710 propagating on flat bottoms including laboratory scale and actual ocean scale, and ISWs over a

711 submerged triangular ridge, a Gaussian ridge and slopes. The following conclusions were obtained as a

712 result of this study.

713 ISWFoam using the finite volume method with unstructured grids and local mesh refinement can

714 accurately simulate the generation and evolution of ISWs, the ISW breaking phenomenon, waveform

715 inversion of ISWs and the interaction between ISWs and complex structures and topography. The

716 method of initializing the ISW using weakly nonlinear eKdV equation models requires a period of

717 movement before the jump of the velocity field develops into a field with continuous changes in velocity.

718 The DJL equation wave generation method that considers the vertical velocity and the horizontal velocity

719 along the vertical gradient is better than the eKdV equation wave generation method that only provides

720 the horizontal average velocity. Using ISWFoam to simulate an ISW with infinite wave length, the metric

721 for the appropriate mesh size is given as follows: the dimensions of the horizontal grid are one-one

722 hundred and fiftieth of the characteristic length, while the vertical grid takes one-twenty fifth of the ISW

723 amplitude.

724

Computer code availability

The ISWFoam code (DOI:10.5281/zenodo.5069480.) developed in this article can be downloaded

for free from https://zenodo.org/record/5069480#.YU1j_GJByHs.

Author contributions

QZ and JL jointly developed this numerical method to calculate internal solitary waves in continuously stratified fluids. JL developed the code. TC performed the computations. QZ and JL jointly analysed the calculation results and wrote the paper together.

Competing interest

The authors of this paper declare that they have no conflicts of interest.

Financial support

This work is supported by grants from the National Key Research and Development Program of China (2017YFC1404200), and the National Natural Science Foundation of China (51509183).

Reference

Alford, M. H., Lien, R. C., Simmons, H., Klymak, J., Ramp, S., Yang, Y. J., Tang, D., and Chang, M. H.: Speed and evolution of nonlinear internal waves transiting the South China Sea, Journal of Physical Oceanography., 40, 1338-1355, doi:10.1175/2010JPO4388.1, 2010.

Alford, M. H., MacKinnon, J. A., Nash, J. D., Simmons, H., Pickering, A., Klymak, J. M., Beitzel, T.: Energy flux and dissipation in Luzon Strait: Two tales of two ridges, Journal of Physical Oceanography., 41, 2211-2222. doi:10.1175/JPOD11073.1, 2011.

Alford, M. H., Peacock, T., MacKinnon, J. A., Nash, J. D., Buijsman, M. C., Centurioni, L. R., Fu, K. H.: The formation and fate of internal waves in the South China Sea, Nature., 521, 65-69, doi:10.1038/nature14399, 2015.

Aghsaee, P., Boegman, L., Lamb, K. G.: Breaking of shoaling internal solitary waves, Journal of Fluid Mechanics., 659, 289. doi:10.1017/S002211201000248X, 2010.

Aghsaee, P., Boegman, L., Diamessis, P. J., Lamb, K. G.: Boundary-layer-separation-driven vortex shedding beneath internal solitary waves of depression, Journal of Fluid Mechanics., 690, 321, doi:10.1017/jfm.2011.432, 2012.

Apel, J., Ostrovsky, L., Stepanyants, Y., Lynch, J.F.: Internal Solitons in the Ocean, Technical Report Woods Hole Oceanographic Institution., doi:10.1575/1912/1070, 2006.

Bardina, J.E., Coakley, T.J., and Huang, P.G.: Turbulence Modeling Validation, Testing, and

Development, NASA TM 110446, NASA Ames Research Center, Moffett Field, Calif. doi: 10.2514/6.1997-2121, 1997.

Bell, J. B. and Marcus, D. L.: A second-order projection method for variable-density flows, Journal of Computational Physics., 101(2), 334-348, doi:10.1016/0021-9991(92)90011-M, 1992.

Brown, D. J. and Christie, D. R.: Fully nonlinear solitary waves in continuously stratified incompressible Boussinesq fluids, Physics of Fluids., 10(10), 2569-2586, doi:10.1063/1.869771, 1998.

Boegman, L. and Stastna, M.: Sediment resuspension and transport by internal solitary waves, Annual review of fluid mechanics., 51, 129-154, doi:10.1146/annurev-fluid-122316-045049, 2019.

Buijsman, M. C., McWilliams, J. C., and Jackson, C. R.: East-west asymmetry in nonlinear internal waves from Luzon Strait, Journal of Geophysical Research: Oceans., 115(C10), doi:10.1029/2009JC006004, 2010.

Cai, S., Xie, J., and He, J.: An overview of internal solitary waves in the South China Sea, Surveys in Geophysics., 33, 927-943, doi:10.1007/s10712-012-9176-0, 2012.

Cheng, M. H., Hwang, R. R., and Hsieh, C. M.: Numerical study on the transformation of an internal solitary wave propagating across a vertical cylinder, Applied Ocean Research., 95, 102016, doi:10.1016/j.apor.2019.102016, 2020.

Choi, W. and Camassa, R.: Fully nonlinear internal waves in a two-fluid system, Journal of Fluid Mechanics., 396, 1-36, doi:10.1017/S0022112099005820, 1999

Deshpande, S. S., Anumolu, L., and Trujillo, M. F.: Evaluating the performance of the two-phase flow solver interFoam, Computational Science. Discovery 5, 014016, 1-36, doi:10.1088/1749-4699/5/1/014016, 2012.

Diamessis, P. J., Domaradzki, J. A., and Hesthaven, J. S.: A spectral multidomain penalty method model for the simulation of high Reynolds number localized incompressible stratified turbulence, Journal of Computational Physics., 202(1), 298-322, doi:10.1016/j.jcp.2004.07.007, 2005.

Ding, W., Ai, C., Jin, S., Lin, J.: Numerical investigation of an internal solitary wave interaction with horizontal cylinders, Ocean Engineering., 208, 107430, doi:10.1016/j.oceaneng.2020.107430, 2020.

Dunphy, M., Subich, C., and Stastna, M.: Spectral methods for internal waves: indistinguishable density profiles and double-humped solitary waves, Nonlinear Processes in Geophysics., 18(3), 351-358, doi:10.5194/npg-18-351-2011, 2011.

Farmer, D. M.and Smith, J. D.: Tidal interaction of stratified flow with a sill in Knight Inlet, Deep Sea Research Part A. Oceanographic Research Papers., 27(3-4), 239-254, doi:10.1016/0198-0149(80)90015-1, 1980.

Fringer, O. B., Gerritsen, M., and Street, R. L.: An unstructured-grid, finite-volume, nonhydrostatic, parallel coastal ocean simulator, Ocean Modelling., 14(3-4), 139-173, doi:10.1016/j.ocemod.2006.03.006, 2006.

Fu, D. M., You, Y. X., and Li, W., Numerical simulation of internal solitary waves with a submerged body in a two-layer fluid, Ocean Engineering (Haiyang Gongcheng)., 37(3), 38-44, 2009.

Gao, X. Y., You, Y. X., Wang, X., Li, W.: Numerical simulation for the internal solitary wave based on

MCC theory, Ocean Engineering (Haiyang Gongcheng)., 30(4), 29-36, 2012.

Grimshaw, R., Pelinovsky, E., Talipova, T., Kurkina, O.: Internal solitary waves: propagation, deformation and disintegration, Nonlinear Processes in Geophysics., 17(6), 633-649, doi:10.5194/npg-17-633-2010, 2010.

Guo, C. and Chen, X.: A review of internal solitary wave dynamics in the northern South China Sea, Progress in Oceanography., 121, 7-23, doi:10.1016/j.pocean.2013.04.002, 2014.

Hallberg, R. and Rhines, P.: Buoyancy-driven circulation in an ocean basin with isopycnals intersecting the sloping boundary, Journal of Physical Oceanography., 26(6), 913-940, doi:10.1175/1520-0485(1996)026<0913:BDCIAO>2.0.CO;2, 1996.

Hallberg, R.: Stable split time stepping schemes for large-scale ocean modeling, Journal of Computational Physics., 135(1), 54-65, doi:10.1006/jcph.1997.5734, 1997.

Helfrich, K. R. and Melville, W. K.: Long nonlinear internal waves, Annu. Rev. Fluid Mech., 38, 395-425, doi:10.1146/annurev.fluid.38.050304.092129, 2006.

Hsieh, C. M., Hwang, R. R., Hsu, J. R. C., Cheng, M. H.: Flow evolution of an internal solitary wave generated by gravity collapse, Applied Ocean Research., 48, 277-291, doi:10.1016/j.apor.2014.10.001, 2014.

Hsieh, C. M., Hwang, R. R., Hsu, J. R. C., Cheng, M. H.: Numerical modeling of flow evolution for an internal solitary wave propagating over a submerged ridge, Wave Motion., 55, 48-72, doi:10.1016/j.wavemoti.2014.12.008, 2015.

Hibiya, T.: The generation of internal waves by tidal flow over Stellwagen Bank, Journal of Geophysical Research: Oceans., 93, 533-542, doi:10.1029/JC093iC01p00533, 1988.

Hu, H. C., Tong, B. and Lou, S. Y.: Nonsingular positon and complexiton solutions for the coupled KdV system, Physics Letters A., 351, 403-412, doi:10.1016/j.physleta.2005.11.047, 2006.

Huthnance, J. M.: Waves and currents near the continental shelf edge, Progress in Oceanography., 10, 193-226, doi:10.1016/0079-6611(81)90004-5, 1981.

Issa, R. I.: Solution of the implicitly discretised fluid flow equations by operator-splitting, Journal of computational physics., 62(1), 40-65, doi:10.1016/0021-9991(86)90099-9, 1986.

Jasak, H.: Error Analysis and Estimation for the Finite Volume Method with Applications to Fluid Flows, Ph.D. thesis. Imperial College London, 1996.

Ko, D. S., Martin, P. J., Rowley, C. D., Preller, R. H.: A real-time coastal ocean prediction experiment for MREA04, Journal of Marine Systems., 69(1-2), 17-28, doi:10.1016/j.jmarsys.2007.02.022, 2008.

Kubota, T., Ko, D. R. S., and Dobbs, L. D.: Weakly-nonlinear, long internal gravity waves in stratified fluids of finite depth, Journal of Hydronautics., 12, 157-165, doi:10.2514/3.63127, 1978.

Lamb, K. G.: Numerical experiments of internal wave generation by strong tidal flow across a finite amplitude bank edge, Journal of Geophysical Research: Oceans., 99, 843-864, doi:10.1029/93JC02514, 1994.

Lamb, K. G. and Yan, L.: The evolution of internal wave undular bores: comparisons of a fully nonlinear

numerical model with weakly nonlinear theory, Journal of physical oceanography., 26(12), 2712-2734, doi:10.1175/1520-0485(1996)026<2712:TEOIWU>2.0.CO;2, 1996.

Lamb, K. G.: A numerical investigation of solitary internal waves with trapped cores formed via shoaling. Journal of Fluid Mechanics, 451, 109-144, doi.org/10.1017/S002211200100636X, 2002.

Lamb, K. G. and Nguyen, V. T.: Calculating energy flux in internal solitary waves with an application to reflectance, Journal of Physical Oceanography., 39, 559-580, doi:10.1175/2008JPO3882.1, 2009.

Lamb, K. G.: Energy and pseudoenergy flux in the internal wave field generated by tidal flow over topography, Continental Shelf Research., 27, 1208-1232, doi:10.1016/j.csr.2007.01.020, 2007.

Lamb K G, Xiao W.: Internal solitary waves shoaling onto a shelf: Comparisons of weakly-nonlinear and fully nonlinear models for hyperbolic-tangent stratifications, Ocean Modelling., 78, 17-34, doi.org/10.1016/j.ocemod.2014.02.005, 2014.

Li, J. Y., Zhang, Q. H., and Chen. T. Q.: Numerical Simulation of Internal Solitary Wave in Continuously Stratified Fluid, Journal of Tianjin University (Science and Technology)., 54(02), 161-170, DOI:10.11784/tdxbz202001025, 2021.

Li, Q. and Farmer, D. M.: The generation and evolution of nonlinear internal waves in the deep basin of the South China Sea, Journal of Physical Oceanography., 41(7), 1345-1363, doi:10.1175/2011JPO4587.1, 2011.

Li, Z., You, Y. U., Zhe, S., Zang, J. M., LI, Z. H., Yu, Z. B.: CFD Simulation of Internal Solitary Wave Using the Volume-of-fluid Method within OpenFOAM, DEStech Transactions on Computer Science and Engineering, doi:10.12783/dtcse/mmsta2017/19617, 2017 (mmsta).

Long, R. R.: Some aspects of the flow of stratified fluids: I. A theoretical investigation, Tellus.,5(1), 42-58, doi:10.3402/tellusa.v5i1.8563, 1953.

Lou, S. Y., Tong, B., Hu, H. C., Tang, X. Y.: Coupled KdV equations derived from two-layer fluids, Journal of Physics A: Mathematical and General., 39, 513, doi:10.1088/0305-4470/39/3/005, 2005.

Meng, Q. and Zhang, C.: A third-order KdV solution for internal solitary waves and its application in the numerical wave tank, Journal of Ocean Engineering and Science., 1(2), 93-108, doi:10.1016/j.joes.2016.03.002, 2016.

Menter, F. R., Kuntz, M., and Langtry, R.: Ten years of industrial experience with the SST turbulence model,Turbulence, heat and mass transfer., 4(1), 625-632, 2003.

Michallet, H. and Ivey, G. N.: Experiments on mixing due to internal solitary waves breaking on uniform slopes, Journal of Geophysical Research: Oceans., 104, 13467-13477, doi:10.1029/1999JC900037, 1999.

Miyata, M.: An internal solitary wave of large amplitude, La Mer. 23, 43-48, 1985.

Miyata, M.: Long Internal Waves of Large Amplitude. Springer, Berlin, pp. 399-406. doi:10.1007/978-3-642-83331-1_44. 1988.

OpenFOAM User Guide 2019 http://www.openfoam:docs/.

OpenFOAM User Guide 2019 http://www.openfoam.com/documentation/user-guide.

Osborne, A. R. and Burch, T. L.: Internal solitons in the Andaman Sea, Science., 208, 451-460,

doi:10.1126/science.208.4443.451, 1980.

Rayson, M. D., Ivey, G. N., Jones, N. L., Fringer, O. B.: Resolving high-frequency internal waves generated at an isolated coral atoll using an unstructured grid ocean model, Ocean Modelling., 122, 67-84, doi:10.1016/j.ocemod.2017.12.007, 2018.

Sandstrom, H. and Elliott, J. A.: Internal tide and solitons on the Scotian Shelf: A nutrient pump at work, Journal of Geophysical Research: Oceans., 89, 6415-6426, doi:10.1029/JC089iC04p06415, 1984.

Seadawy, A. R.: Exact solutions of a two-dimensional nonlinear Schrödinger equation, Applied Mathematics Letters., 25, 687-691, doi:10.1016/j.aml.2011.09.030, 2012.

Seadawy, A. R., Lu, D., and Yue, C.: Travelling wave solutions of the generalized nonlinear fifth-order KdV water wave equations and its stability, Journal of Taibah University for Science., 11, 623-633, doi:10.1016/j.jtusci.2016.06.002, 2017.

Shaw, P. T., Ko, D. S., and Chao, S. Y.: Internal solitary waves induced by flow over a ridge: With applications to the northern South China Sea, Journal of Geophysical Research: Oceans., 114(C2), doi:10.1029/2008JC005007, 2009.

Simmons, H. L., Hallberg, R. W., and Arbic, B. K.: Internal wave generation in a global baroclinic tide model, Deep Sea Research Part II: Topical Studies in Oceanography., 51(25-26), 3043-3068, doi:10.1016/j.dsr2.2004.09.015, 2004.

Smedstad, O. M., Hurlburt, H. E., Metzger, E. J., Rhodes, R. C., Shriver, J. F., Wallcraft, A. J., Kara, A. B.: An operational eddy resolving 1/16 global ocean nowcast/forecast system,Journal of Marine Systems.,40, 341-361, doi:10.1016/S0924-7963(03)00024-1, 2003.

Subich, C. J., Lamb, K. G., and Stastna, M.: Simulation of the Navier–Stokes equations in three dimensions with a spectral collocation method, International Journal for Numerical Methods in Fluids., 73(2), 103-129, doi:10.1002/fld.3788, 2013.

Thiem, Ø., Carr, M., Berntsen, J., Davies, P. A.: Numerical simulation of internal solitary wave-induced reverse flow and associated vortices in a shallow, two-layer fluid benthic boundary layer. Ocean dynamics., 61, 857, doi:10.1007/s10236-011-0396-5, 2011.

Turkington, B., Eydeland, A., and Wang, S.: A computational method for solitary internal waves in a continuously stratified fluid, Studies in Applied Mathematics., 85, 93-127, doi:10.1002/sapm199185293, 1991.

Vlasenko, V., Stashchuk, N., and Hutter, K.: Baroclinic Tides: Theoretical Modeling andObservational Evidence, Cambridge University Press., doi:10.5670/oceanog.2006.107, 2005.

Vlasenko, V., Stashchuk, N., Guo, C., Chen, X.: Multimodal structure of baroclinic tides in the South China Sea, Nonlinear Processes in Geophysics., 17(5), 529-543, doi:10.5194/npg-17-529-2010, 2010.

Wang, X., Zhou, J. F., Wang, Z., You, Y. X.: A numerical and experimental study of internal solitary wave loads on semi-submersible platforms, Ocean Engineering., 150, 298-308, doi:10.1016/j.oceaneng.2017.12.042, 2018.

Wilcox, D. C.: Comparison of two-equation turbulence models for boundary layers with pressure

gradient, AIAA journal., 31(8), 1414-1421, doi:10.2514/3.11790, 1993.

Xu, C. and Stastna, M.: Instability and cross-boundary-layer transport by shoaling internal waves over realistic slopes, Journal of Fluid Mechanics., 895, doi:10.1017/jfm.2020.389, 2020.

Yuan, G. and Xiao-Yan, T.: A coupled variable coefficient modified KdV equation arising from a two-layer fluid system, Communications in Theoretical Physics., 48, 961-970, doi:10.1088/0253-6102/48/6/001, 2007.

Zhang, Z., Fringer, O. B., and Ramp, S. R.: Three-dimensional, nonhydrostatic numerical simulation of nonlinear internal wave generation and propagation in the South China Sea, Journal of Geophysical Research: Oceans., 116(C5), doi:10.1029/2010JC006424, 2011.

Zhang. H. G., Gu J. B., Jia, H. Q., Gu, B.: A numerical model for internal wave propagation in continuously stratified ocean, Chinese Journal of Theoretical and Applied Mechanics., 44, 896-903, doi:10.6052/0459-1879-12-195, 2012.